arXiv:1902.08123v1 [cs.CV] 21 Feb 2019

# Cross-Sensor Periocular Biometrics: A Comparative Benchmark including Smartphone Authentication

Fernando Alonso-Fernandez[a,*], Kiran B. Raja[b], R. Raghavendra[b], Cristoph Busch[b], Josef Bigun[a], Ruben Vera-Rodriguez[c], Julian Fierrez[c]

[a] *School of Information Technology, Halmstad University, Sweden*
[b] *Norwegian University of Science and Technology, Gjøvik, Norway*
[c] *School of Engineering, Universidad Autonoma de Madrid, Spain*

**Abstract**

The massive availability of cameras and personal devices results in a wide variability between imaging conditions, producing large intra-class variations and a significant performance drop if images from heterogeneous environments are compared for person recognition purposes. However, as biometric solutions are extensively deployed for person recognition, it will be common to replace acquisition hardware as it is damaged or newer designs appear, or to exchange information between agencies or applications operating in different environments. Furthermore, variations in imaging spectral bands can also occur. For example, face images are typically acquired in the visible (VW) spectrum, while iris images are usually captured in the near-infrared (NIR) spectrum. However, cross-spectrum comparison may be needed if for example a face image obtained from a surveillance camera needs to be compared against a legacy database of iris imagery. Here, we propose a multialgorithmic approach to cope with cross-sensor periocular recognition. We integrate different systems using a fusion scheme based on linear logistic regression, in which fused scores tend to be log-likelihood ratios. This allows easy combination by just summing scores of available systems. We evaluate our approach in the context of the 1st Cross-Spectral Iris/Periocular Competition, whose aim was to compare person recognition approaches when periocular data from visible

*Corresponding author
*Email addresses:* feralo@hh.se (Fernando Alonso-Fernandez), kiran.raja@ntnu.no (Kiran B. Raja), raghavendra.ramachandra@ntnu.no (R. Raghavendra), christoph.busch@ntnu.no (Cristoph Busch), josef.bigun@hh.se (Josef Bigun), ruben.vera@uam.es (Ruben Vera-Rodriguez), julian.fierrez@uam.es (Julian Fierrez)

and near-infrared images is matched. The proposed fusion approach achieves reductions in the error rates of up to 20-30% in cross-spectral NIR-VW comparisons, leading to an EER of 0.22% and a FRR of just 0.62% for FAR=0.01%, representing the best overall approach of the mentioned competition.. Experiments are also reported with a database of VW images from two different smartphones, achieving even higher relative improvements in performance. We also discuss the proposed approach from the point of view of template size and computation times, with the most computationally heavy system playing an important role in the results.

*Keywords:* Periocular recognition, interoperability, cross-spectral, cross-sensor, fusion, linear logistic regression.

---

## 1. Introduction

Periocular biometrics has gained attention as an independent modality for person recognition [1] after concerns of the performance of face or iris modality under non-ideal conditions [2, 3]. Periocular refers to the face region in the immediate vicinity of the eye, including the sclera, eyelids, eyelashes, eyebrows and the surrounding skin. With a surprising high discrimination ability, it is the ocular modality requiring the least constrained acquisition. It appears over a wide range of distances, even under partial face occlusion (close distance) or low resolution iris (long distance), facilitating increased performance in unconstrained or uncooperative scenarios. It also avoids the need of iris segmentation, an issue in difficult images [4]. Another advantage is that the periocular region appears in iris and face images, so it can be easily obtained with existing setups for face and iris.

Ocular biometrics has seen significant progress in the last decade, primarily due to efforts in iris recognition since late 80s, resulting in large-scale deployments [5]. Iris provides very high accuracy in near infrared (NIR) lightning, but deployment to non-controlled environments is not yet mature [6]. The fast-growing uptake of face technologies in social networks and smartphones, as well as the widespread use of surveillance cameras, arguably increases the interest of periocular biometrics, specially in the visible (VW) range. In this context, samples captured with different sensors are

to be compared if, for example, users are allowed to use their own acquisition cameras. This massive availability of devices results in heterogeneous quality between images [7], which is know to decrease recognition performance significantly [8]. This *cross-sensor* issue also arises when a biometric sensor is replaced with a newer one without reacquiring the corresponding template, thus forcing biometric samples from different sensors to co-exist. In addition, iris images are largely acquired beyond the visible spectrum [9], but there are several scenarios in which it may be necessary to compare them with periocular images in VW range (*cross-spectral* comparison), as for example in law enforcement scenarios where the only available image of a suspect is obtained with a surveillance camera [10, 11]. These *interoperability* problems, if not properly addressed, can affect the recognition performance dramatically. Unfortunately, widespread deployment of biometric technologies will inevitably cause the replacement of hardware parts as they are damaged or newer designs appear, or to exchange information among agencies or applications which employ different technological solutions or whose data is captured in heterogeneous environments.

In this paper, we combine periocular recognition systems at score level, referred to as multialgorithm fusion (in contrast to multimodal fusion, which combines information from different modalities) [12, 13]. The consolidation of identity evidence from heterogeneous algorithms or systems (also called experts in the present paper) is known to increase recognition performance, because the different sources can compensate for the limitations of the others [12, 14]. Integration at the score level is the most common approach, because it only needs the output scores of the different systems, greatly facilitating the integration. With this motivation, we propose a multialgorithm fusion approach for cross-sensor periocular recognition which integrates different feature methods. It follows a probabilistic fusion approach based on linear logistic regression [15], in which scores of each individual system are mapped to a log-likelihood ratio according to a probabilistic Bayesian framework, allowing easy interpretation and efficient combination of scores from different modalities. The described approach was submitted to the $1^{st}$ Cross-Spectral Iris/Periocular Competition (Cross-Eyed 2016) [16], with outstanding recognition accuracy (Equal Error Rate of 0.29%, and 0% False Rejection Rate at a False Acceptance Rate of 0.01%), resulting the best overall com-

peting approach.. This competition was aimed at evaluating the capability of periocular recognition algorithms to compare visible and near-infrared images. We also carry out experiments with periocular images in visible range, but with two different sensors. For this purpose, we employ a database captured with two different smartphones [17], demonstrating the benefits of the proposed approach to this particular problem as well.

This paper is organized as follows. This introduction is completed with the description of the paper contributions, and a summary of related works in periocular biometrics. Section 2 then describes the periocular recognition systems employed. Cross-spectral (NIR-VW) and cross-sensor (VW-VW) recognition experiments are described in Sections 3 and 4, respectively, including the databases, protocol used, results of the individual experts, and fusion experiments. Finally, conclusions are given in Section 5.

### *1.1. Contributions*

The contribution of this paper to the state of the art is thus as follows. First, we summarize related works in cross-sensor periocular recognition. Second, we comparatively evaluate seven periocular recognition algorithms under the frameworks of cross-spectral NIR-VW and cross-sensor smartphone recognition. The Reading Cross-Spectral Iris/Periocular Dataset [16] and the Visible Spectrum Smartphone Iris (VSSIRIS) [17] databases are respectively used for this purpose (see Figure 1). We employ the three most widely used features in periocular research [18], three self-developed algorithms [19, 20, 21], and one comparator based on Convolutional Neural Networks [22]. The comparison is done both in terms of performance, and of template size and computation times. Third, we describe our multialgorithm fusion architecture for cross-sensor periocular recognition. Since the scores output by the various experts are heterogeneous, score normalization is needed to transform these scores into a common domain prior to the fusion process [12]. We solve this problem by linear logistic regression fusion [23, 24], a trained classification approach which does not need any prior normalization stage. Instead, the score of each single expert is mapped to be a log-likelihood ratio. This is the logarithm of the ratio between the likelihood that input signals were originated by the same subject, and the likelihood that input signals were not originated by the same subject. This form of output is expert-independent, in the

sense that this log-likelihood-ratio output can theoretically be used to make optimal (Bayes) decisions; in addition, under independence assumptions (as in the case of different feature extraction methods), the sum of log-likelihood ratios results in another log-likelihood ratio [25], thus providing a simple fusion framework by simply summing the score given by each available system. An additional advantage is that since scores of each expert are trained separately, there is no need to retrain the whole fusion algorithm again if the number of available systems change. If a new system is added, it is only necessary to train the mapping function of that particular algorithm only, and just sum the resulting score to the scores of the other available experts. Conversely, if a system becomes unavailable or unreliable, its score is simply ignored. Fourth, in our experiments, conducted according to the 1st Cross-Spectral Iris/Periocular Competition (Cross-Eyed 2016) [16], reductions of up to 20-30% in the error rates are obtained by fusion under NIR-VW comparison, resulting in a cross-spectral EER of 0.22% and a FRR @ FAR=0.01% of just 0.62%, the best overall approach in the mentioned competition. Regarding cross-sensor smartphone recognition, reductions in error rates achieve 38/73% in EER/FRR respectively, with corresponding cross-sensor error values of 1% (EER) and 3.4% (FRR). This fusion approach has been previously applied successfully to cross-sensor comparison in face and fingerprint modalities [15], which excellent results in other competition benchmarks as well [26].

### *1.2. Related Works in Cross-Sensor Periocular Biometrics*

Interoperability between different sensors are of high interest in new scenarios arising from the widespread use of biometric technologies and the availability of multiple sensors and vendor solutions. Cross-sensor comparison of images in the visible range from smartphone sensors is carried out for example in [27, 28, 29]. In the work [28], the authors apply Laplacian decomposition of the image coupled with dynamic scale selection, followed by frequency decomposition via Short-Term Fourier Transform. The database employed is the MICHE I dataset [30], which contains 75 subjects captured with the front and rear cameras of two smartphones. The cross-sensor performance obtained (EER) ranges from 6.38 to 8.33% for the different combinations of reference and probe cameras. The authors in [27] use a sensor-specific color correction tech-

nique, which is estimated by using a color chart in a dark acquisition scene that is further illuminated by a standard illuminant. The authors also carry out score-level fusion of six iris and five periocular systems, which is done by Neural Networks. They also presented a new database (CSIP), with images from 50 subjects captured with four different smartphones in ten different setups (based on the use of frontal/rear camera and flash/no flash). The best reported periocular performance by fusion of the five available systems is EER=15.5%. The same database is also employed in [29], where the authors apply three different methods to solve the cross-sensor task: GMM-universal background models (GMM-UBM), GMM supervectors (SV-SDA), and deep transfer learning (CNN). They achieve a rank-1 recognition rate of 93.3% in the best possible case. The work [31], on the other hand, addressed the issue of cross-sensor recognition in the NIR spectrum, using self-captured images from three different sensors. Sensor interoperability is dealt with by weighted fusion of information from multiple directions of Ordinal Measures, with a reported cross-sensor performance (EER) between 20 and 28%.

Regarding cross-sensor recognition across different spectra, the work [10] proposes to compare the ocular region cropped from VW face images against NIR iris images, since face images are usually captured in the visible range, while iris images in commercial systems are usually acquired using near-infrared illumination. They employ three different feature descriptors, namely Local Binary Patterns (LBP), Normalized Gradient Correlation (NGC), and Joint Database Sparse Representation (JDSR). Using a self-captured database, they report a cross-spectral performance of EER=23% by score-level fusion of the three experts.

In another line of work, surveillance at night or in harsh environments has prompted interest in new imaging modalities. For example, the authors in [32] presented the IIITD Multispectral database (IIITD-IMP), with VW, NIR and Night Vision images from 62 subjects (the latter captured with a video camera in Night Vision mode). To cope with cross-spectral periocular comparisons, they employ Neural Networks to learn the variabilities caused by each pair of spectra. The employed descriptor is a Pyramid of Histogram of Oriented Gradients (PHOG) [33], which is used as input of the Neural Networks. Reported cross-spectral performance is between FRR=52.9% and

FRR=20% at FAR=1%. The authors in [34] employed the IIITD Multispectral and the PolyU database (with 209 subjects) to carry out VW-to-NIR comparison. They used Markov Random Fields combined with two different experts, variants of local binary patterns (LBP), namely, FPLBP (Four-Patch LBP) and TPLBP (Three-Patch LBP). They reported a Genuine Accept Rate (GAR) at a 0.1% False Acceptance Rate (FAR) of 16-18% (IIITD-IMP) and 45-73% (PolyU). These two databases, together with the Cross-Eyed database (with 120 subjects) [16] were used in the work [35]. To normalize the differences in illumination between NIR and VW images, they applied Difference of Gaussian (DoG) filtering. The descriptor employed is the Histogram of Oriented Gradients (HOG). The IIITD-IMP produces the worst results, with a cross-spectral EER of 45% and a GAR at 0.1% FAR of only 25%. The reported accuracy with the other databases is better, ranging between 10-14% (EER) and 83-89% (GAR).

Latest advancements have resulted in devices with ability to see through fog, rain, at night, and to operate at long ranges. In the work [36], the authors carry out experiments with different wavelengths, namely VW, NIR, SWIR (ShortWave Infrared), and MWIR (MiddleWave Infrared. In the mentioned paper, they use images captured at distances of 1.5 m, 50 m, and 105 m. Feature extraction is done with a bank of Gabor filters, with the magnitude and phase responses further encoded with three descriptors: Weber Local Descriptor (WLD) [37], Local Binary Patterns (LBP) [38], and Histogram of Oriented Gradients (HOG) [39]. Extensive experiments are done in this work between the different spectra and standoff distances. Recently, the work [40] presented a new multispectral database captured in eight bands across VW and NIR spectrum (530 to 1000 nm). 52 subjects were acquired using a custom-built sensor which captures ocular images simultaneously in the eight bands. The descriptors evaluated were Histogram of Oriented Gradients (HOG), perceptual descriptors (GIST), Log-Gabor filters (LG), and Binarized Statistical Image Features (BSIF). The cross-band accuracy varied greatly depending on the reference and probe bands, ranging from 8.46% to 91.92% rank-1 recognition rate.

## 2. Periocular Recognition Systems

This section describes the machine experts used for periocular recognition. We employ the most widely used features in periocular research [1]: Histogram of Oriented Gradients (HOG) [39], Local Binary Patterns (LBP) [38], and Scale-Invariant Feature Transform (SIFT) keypoints [41], as well as three self-developed algorithms based on Symmetry Descriptors (SAFE) [19], Gabor features (GABOR) [20], and Steerable Pyramidal Phase Features (NTNU) [21]. We also employ a machine expert based on the VGG-Face Convolutional Neural Network (VGG) [22].

### *2.1. Based on Symmetry Patterns (SAFE)*

This system employs the Symmetry Assessment by Feature Expansion (SAFE) descriptor [19], which encodes the presence of various symmetric curve families around image key-points (Figure 2, top). We use the eye center as unique key-point for feature extraction. The system starts by extracting the complex orientation map of the image, via symmetry derivatives of Gaussians [42], as shown in Figure 3. We employ $S$=6 different standard deviations (according to [41]) in computing the orientation map, therefore capturing features at different scales. For each scale, we then project $N_f = 3$ ring-shaped areas of different radii around the eye center onto an space of $N_h = 9$ harmonic functions. We use the result of scalar products of harmonic filters (Figure 2, bottom) with the orientation image to quantify the amount of presence of different symmetric pattern families within each annular band. The resulting complex feature vector is given by an array of $S \times N_h \times N_f$ elements. The comparison score $M \in \mathbb{C}$ between two SAFE arrays is computed using the triangle inequality. Argument $\angle M$ represents the angle between the two arrays (expected to be zero when the symmetry patterns detected coincide for reference and test feature vectors, and 180° when they are orthogonal), and the confidence is given by $|M|$. To include confidence into the angle difference, we use $MS = |M| \cos \angle M$, with the resulting score $MS \in [-1, 1]$.

The annular band of the first ring is set in proportion to the distance between eye corners (Cross-Eyed database) or to the radius of the sclera circle (VSSIRIS database), while the band of the last ring ends at the boundary of the image. This difference

in setting the smallest ring is due to the ground-truth information available for each database, as will be explained later in the respective sections. The ROI of the SAFE expert is shown in Figure 1 (third column). Using the eye corners or the sclera boundary as reference for annular bands alleviates the effect of dilation that affects the pupil, because they are not affected by such dilation, therefore capturing the same relative regions across different images.

### *2.2. Based on Gabor Features (GABOR)*

This expert is described in [20], which is based on the face detection and recognition system of [43]. The periocular image is decomposed into non-overlapped square regions (Figure 1, fourth column), and the local power spectrum is then sampled at the center of each block by a set of Gabor filters organized in 5 frequency and 6 orientation channels. An example of Gabor filters is shown in Figure 4. This sparseness of the sampling grid allows direct Gabor filtering in the image domain without needing the Fourier transform, with significant computational savings and feasibility in real time. Gabor responses from all grid points are grouped into a single complex vector, and the comparison between two images is done using the magnitude of complex values via the $\chi^2$ distance. Prior to the comparison with magnitude vectors, they are normalized to a probability distribution (PDF). We employ the $\chi^2$ distance because it has been observed to produce better results than other distances when using normalized histograms.

### *2.3. Based on Steerable Pyramidal Phase Features (NTNU)*

Image features from multi-scale pyramids have proven to extract discriminative features in many earlier works including applications to texture synthesis, texture retrieval, image fusion, and texture classification among others [44, 45, 46, 47, 48, 49, 50, 51]. Inspired by the applicability of extracted discriminative features, in this work, we employ steerable pyramidal features for the task of cross-sensor periocular image classification. Further, observing the nature of textures that are different across spectrum (NIR versus VW), we propose to employ the quantized phase information from the multi-scale pyramid of the image, as explained further.

A steerable pyramid is a translation and rotation invariant transform in a multi-scale, multi-orientation and self-inverting image decomposition into a number of sub-bands [52, 53, 54]. The pyramidal decomposition is performed using directional derivative operators of a specific order. The key motivation in using steerable pyramids is to obtain both linear and shift-invariant features in a single operation. Further, the choice of steerable pyramids is that they not only provide multi-scale decomposition of images, but also provide the advantages of orthonormal wavelet transforms that are both localized in space and spatial-frequency with aliasing effects [52]. The basis functions of the steerable pyramid are $K$-order directional derivative operators. For any choice of $K$, the steerable pyramids come in different scales and $K + 1$ orientations.

For a given input image, the features of steerable pyramid coefficients can be represented using $S_{(m,\theta)}$, where $m$ represents the scale and $\theta$ represents the orientation. In this work, we generate a steerable pyramid with 3 scales ($m \in \{1, 2, 3\}$) and angular coefficients in the range $\theta_1 = 0$ to $\theta_{K+1} = 360$, resulting in a pyramid which covers all directions. The set of sub-band images corresponding to one scale in the multi-scale pyramidal decomposition can be therefore represented as $S_m = \{S_{(m,\theta_1)},\ S_{(m,\theta_2)}, \ldots S_{(m,\theta_{K+1})}\}$.

Considering the features from multi-scale decomposition, we further note that the textural information represented is different in the NIR and VW domains. In order to address this limitation and obtain domain invariant features, we propose to extract the local phase features [55] from each sub-band image $S_{(m,\theta)}$ in a local region $\omega$ in the neighbourhood of $n$ pixels given by:

$$F_{(m,\theta)}(u, x) = S_{(m,\theta)}(x, y)\omega_R(y - x) \exp\{-j2\pi U^T y\} \tag{1}$$

where $x, y$ represent the pixel location. Further, the local phase response obtained through Fourier coefficients are computed for the frequency points $u_1, u_2, u_3$ and $u_4$, which relate to four points $[a, 0]^T, [0, a]^T, [a, a]^T, [a, -a]^T$ such that the phase response $H(u_i) > 0$ [55]. The phase information presented in the form of Fourier coefficients is then separated into real and imaginary parts of each component, as given by $[Re\{F\}, Im\{F\}]$, to form a vector $R$ with eight elements. Next, the elements $R_i$ of $R$ are binarized and quantized by assigning a value of 1 for all components with response

greater than 1 and 0 otherwise, as given in Equation 2.

$$Q_i = \begin{cases} 1, & \text{if } R_i > 0 \\ 0, & \text{otherwise} \end{cases} \tag{2}$$

The quantized phase information is finally encoded to form a compact pixel representation $P$ in the $0-255$ range by using simple binary to decimal conversion strategy as given by Eqn. 3.

$$P_{(m,\theta)} = \sum_{j=1}^{8} Q_j \times (2^{(j-1)}) \tag{3}$$

This procedure is followed with the different scales and orientations of the selected space. All the phase responses $P_{(m,\theta)}$ obtained by such scales and orientations are concatenated into a single vector, which is used as feature representation of the input image. Comparison between feature representations of two images is done using the $\chi^2$ distance.

### *2.4. Based on SIFT Key-points (SIFT)*

This system is based on the SIFT operator [41]. SIFT keypoints are extracted in the annular ROI shown in Figure 1, third column. The recognition metric between two images is the number of paired keypoints, normalized by the minimum number of detected keypoints in the two images under comparison. We use a free C++ implementation of the SIFT algorithm[1], with the adaptations described in [56]. Particularly, it includes a post-processing step to remove spurious pairings using geometric constraints, so pairs whose orientation and length differ substantially from the predominant orientation and length are removed.

### *2.5. Based on Local Binary Patterns (LBP) and Histogram of Oriented Gradients (HOG)*

Together with SIFT key-points, LBP [38] and HOG [39] have been the most widely used descriptors in periocular research [1]. An example of LBP and HOG features is

[1] http://vision.ucla.edu/∼vedaldi/code/sift/assets/sift/index.html

shown in Figure 5. The periocular image is decomposed into non-overlapped regions, as with the Gabor system (Figure 1). Then, HOG and LBP features are extracted from each block. Both HOG and LBP are quantized into 8 different values to construct an 8 bins histogram per block. Histograms from each block are then normalized to account for local illumination and contrast variations, and finally concatenated to build a single descriptor of the whole periocular region. Image comparison with HOG and LBP can be done by simple distance measures. Euclidean distance is usually used for this purpose [18], but here we employ the $\chi^2$ distance for the same reasons than with the Gabor system.

### *2.6. Based on Convolutional Neural Networks (VGG)*

This system is based on the VGG-Face Convolutional Neural Network [22], which is implemented using $\sim$1 million images from the Labeled Faces in the Wild [57] and YouTube Faces [58] datasets. Since it is originally trained for classifying faces, we believe that it can provide effective recognition with the periocular region as well. Based on the study [59], we employ the pre-trained VGG-Face architecture. Periocular images are fed into the feature extraction pipeline of the CNN, but instead of using the vector from the last layer, we employ as feature descriptor the vector from the intermediate layer identified in [59] as providing the best performance with periocular images. In case of VGG-Face, the best layer is found to be the layer 25, see [59] for further details. This approach allows the use of powerful deep-learning architectures pre-trained with a large number of images in a related domain, but without the need of re-training. Training a new architecture may be unfeasible if there is a lack of large-scale data in the target domain, which is the case in cross-sensor periocular recognition. The extracted CNN vectors can be simply compared with distance measures. In our case, we employ the $\chi^2$ distance.

## 3. Cross-Spectral Periocular Recognition

### *3.1. Database and Protocol*

In the cross-spectral recognition experiments of this section, we employ the Reading Cross-Spectral Iris/Periocular Dataset used as the benchmark dataset for the $1^{st}$

Cross-Spectral Iris/Periocular Competition (Cross-Eyed 2016) [16]. The dataset contains both visible (VW) and near-infrared (NIR) images captured with a custom dual spectrum imaging sensor which acquires images in both spectra synchronously. Periocular images are of size $800 \times 900$ (height$\times$width) from 120 subjects, with 8 images of both eyes captured in both spectra, totalling 3840 images. Images are captured at a distance of 1.5 m, in uncontrolled indoor environment, containing large variations in ethnicity, eye color, and illumination reflections. Some examples are shown in Figure 6 (top). To avoid usage of iris information by periocular methods during the Cross-Eyed competition, periocular images are distributed with a mask on the eye region, as discussed in [18].

Prior to the competition, a *training* set comprising images from 30 subjects was distributed to the participants to tune their algorithms. The *test* set of the evaluation consisted of images from 80 subjects, which were sequestered by the organizers, and distributed after the competition was finished. Images from 10 additional subjects were also released after the competition that were not present in the test set. Here, we will employ the same 30 subjects of the training set to tune our algorithms, and the remaining 90 subjects for testing purposes. All images have an annotation mask of the eye region, which is used as input for our experiments. The mass center of the mask is set as the reference point (center) of the eye. All images are then rotated w.r.t. the axis that crosses the two sclera corners, and resized via bicubic interpolation to have the same corner-to-corner distance (set empirically to 318 pixels, average distance value of the training set). Then, images are aligned by extracting a region of $613 \times 701$ around the eye. This size is set empirically to ensure that all available images have sufficient margin to the four sides of the eye center. Eyes in the Cross-Eyed database are slightly displaced in vertical direction, so the eye is not centered in the aligned images but with a vertical offset of 56 pixels (see Figure 1). Images are further processed by Contrast Limited Adaptive Histogram Equalization (CLAHE) [60], which is the preprocessing choice with ocular images [61], and then sent to feature extraction.

We carry out verification experiments, with each eye considered a different user. We compare images both from the same device (*same-sensor*) and from different devices (*cross-sensor*). Genuine trials are obtained by comparing each image of an eye

to the remaining images of the same eye, avoiding symmetric comparisons. Impostor trials are done by comparing the $1^{st}$ image of an eye to the $2^{nd}$ image of the remaining eyes. To increase the number of available training scores, we carry out an additional comparison to the $3^{rd}$ image of the remaining eyes only with the training set. The experimental protocol is summarized in Table 1.

The periocular experts employed have some parameters that are dependant of the image size. Regarding the SAFE descriptor, the annular band of the first circular ring starts at a radius of $R$=79 pixels (determined empirically as 1/4 of the eye corner-to-corner distance), and the band of the last ring ends at the bottom boundary of the image. This results in a ROI of $501 \times 501$ pixels around the eye center (Figure 1, third column). The grid employed with GABOR, LBP and HOG systems has $7 \times 8$=56 blocks of $88 \times 88$ pixels; however, the 8 central blocks containing the eye region mask are not considered, therefore features are extracted only from 48 blocks. The GABOR operator employs filter wavelengths spanning from 44 to 6 pixels, which are set proportional to the block size as 88/2=44 to $88/16 \approx 6$ (Figure 4). The VGG system employs an input image size of $224 \times 224$, so images are resized to match these dimensions. Table 2 (top) indicates the size of the feature vector for a given periocular image with the different systems employed. Experiments have been done in a Dell Latitude E7240 laptop with an i7-4600 (2.1 GHz) processor, 16 Gb DDR3 RAM, and a built-in Intel HD Graphics 4400 card. The OS is Microsoft Windows 8.1 Professional, and the algorithms are implemented in Matlab r2018b x64, with the exception of SIFT that is implemented in C++ and invoked from Matlab via MEX files. The VGG-Face model is from Caffee, which has been imported to Matlab with the `importCaffeNetwork` function. The size of stored template files, and the extraction and comparison times are given in Table 3 (top).

### *3.2. Results: Individual Systems*

The performance of individual systems is reported in Figure 7 and Table 4. Besides the Equal Error Rate, we also report the False Rejection Rate (FRR) at a False Acceptance Rate (FAR) of 0.01%. This is because the latter was the metric used to rank submissions to the Cross-Eyed competition. We report three types of results: $i$)

*same-sensor* comparisons; $ii$) *cross-sensor* comparisons; and $iii$) *overall* (scores from $i$ and $ii$ pooled together). In Figure 8, we also provide the cross-sensor verification accuracy of each system against its template size.

Based on results of the SIFT expert ($\sim$0% error in same-sensor comparisons), we also carry out experiments with 200 key-points per image only (denoted as 200p), which are extracted by changing iteratively the threshold to exclude low contrast points. Limiting the number of key-points when image resolution increases has been also observed in other periocular studies [62]. In this paper, we use the SIFT detector with the same parametrization employed in [56] for iris images of size 640$\times$480. In the work [56], the iris region represented $\sim$1/8 of the image only, leading to some hundreds of key-points per image. However, images of the Cross-Eyed database are of 613$\times$701 pixels, and the periocular ROI occupies a considerable bigger area than the iris region, leading to an average of $\sim$1900 key-points per image. While it allows a nearly zero error, the template model has around 1 MB, and the average comparison time is 0.58 sec on a laptop with a C++ implementation (Table 3), which may not be feasible when transferred to smartphones or other devices having limited capabilities. Comparison time is one of the drawbacks of key-point based systems, since it is usually needed to compare each key-point of one image against all key-points of the other image to find a pair match, thus increasing the computation time exponentially when the number of key-points per image increases [1]. The other systems employed have templates of fixed size, thus comparison is done very efficiently using distance measures involving a number of fixed calculations. It should be also be taken into consideration that experiments here are done in a laptop, so increases in computation times are expected if transferred to a smartphone or similar devices.

From Figure 7, it can be seen that all periocular experts have equivalent performance with NIR and VW data (red and green curves). Appreciable differences are only found at low FRR regions, but there is not a consistent tendency between comparators. For example, SAFE, LBP, NTNU and VGG perform better with NIR images in this region, while GABOR and HOG perform better with VW images. In previous studies, the periocular modality usually performs better with VW data [63, 64, 65], so it is generally accepted this modality is most suited to VW imagery [1]. On the contrary,

some other works show opposite results [32]. It should be noted, however, that in the mentioned studies, the images employed are of smaller size, ranging from $100\times160$ to $640\times480$, while the images employed in this paper are of $613\times701$ pixels. Also, they evaluate three different periocular experts at most. In the present paper, the use of bigger images may be the reason of a comparable performance between NIR and VW images.

Regarding cross-sensor experiments, we observe a significant worsening in performance w.r.t. same-sensor comparisons, although not all systems are affected in the same way. The different regions of the DET are not equally affected either. HOG, NTNU and specially LBP, suffer a significant worsening of the performance in high-security mode (i.e. at low FAR), as can be appreciated in the DET curves. The relative FRR increase @ FAR=0.01% for these systems is in the range of 200% to nearly 500% (Table 4). This effect is not so prominent with SAFE, GABOR and VGG. It is also worth noting the increase in error rates suffered by the SIFT comparator under cross-sensor experiments in all its variations, which is significantly higher than any other comparator, despite using a descriptor of bigger size (Table 3). This indicates that the image properties measured by this feature extractor do not remain consistent across NIR and VW spectra to the same extent that with the other systems. The global nature of all the other comparators (which extract features from the whole ROI instead from a discrete set of key-points) may help to alleviate the differences produced by different imaging spectra.

Concerning individual performance of each system, SIFT exhibits very low error rates, at the expense of a much bigger template and comparison time. Limiting the SIFT template to 200 keypoints per image increases error rates approximately one order of magnitude. But even in this case, SIFT is better than most of the other comparators (given that its template size and comparison time is still one or two orders of magnitude larger). In general, there is an inverse proportion between the error rates and the template size, as it can be observed in Figure 8. A remarkable exception is NTNU, whose performance is among the best but its template size is among the smallest. At low FAR, its performance stands out even more w.r.t. the rest of the systems. HOG also shows a good performance despite having a template which is even smaller than

NTNU. The LBP system also has a good EER metric given its small template size, although it shows a significant drop in performance in low FAR regions, being surpassed by the other systems. On the other side of the spectrum is VGG, which comparatively has a big template, but its performance is at the same level of other lighter systems such as NTNU or HOG. It is also worth noting the comparable performance of SAFE w.r.t. GABOR expert, which has a template ten times bigger; however, SAFE has a higher extraction time, since convolution filters are comparable in size to the image ROI ($501 \times 501$). Nevertheless, filter separability with this expert could be explored for faster processing [19].

### *3.3. Results: Fusion of Periocular Systems*

We then carry out fusion experiments using all the available systems. The score of each individual system is mapped to a log-likelihood ratio according to the probabilistic Bayesian framework of [15], and then all scores are summed. Under independence assumptions (such as using systems based on different features), the sum of log-likehood ratios results in another log-likelihood ratio [25], providing a simple fusion framework by simply summing the score given by each individual system. This allows an easy interpretation of the resulting score as well, i.e. higher than zero supports the *same-user* assumption, while lower than zero represents the *different-user* assumption. It also allows to cope easily with a variable number of comparators, since the addition of a new one only requires to train its own mapping function. The resulting fused score is further normalized to the $[0, 1]$ range via the sigmoid function. The mapping function of each system is computed with training scores both from same-sensor and cross-sensor comparisons [15], so both types are taken into account for the mapping. Results are then reported using scores from the test set, with no scores from the test set used to train the fusion functions.

We have tested all the possible fusion combinations, with the best results reported in Tables 5 and 6. Following the protocol of the Cross-Eyed 2016 evaluation, the best combinations are chosen based on the lowest cross-sensor FRR @ FAR=0.01%. As it can be observed, cross-sensor performance is improved significantly by fusion if the SIFT expert is involved. If we allow SIFT to employ all available points (Table 5. top),

reductions of 20-30% are obtained in the EER and FRR. Relative improvements are even higher when employing SIFT with 200 key-points, although in these cases, absolute performance figures are worse due to the worse performance of the SIFT expert when the number of key-points is limited. If we remove the computationally heavier SIFT expert (Table 6), the best cross-sensor performance achievable by fusion is one order of magnitude worse than the best case with SIFT, so it seems that SIFT features contribute decisively to a much smaller error rates. However, even without the SIFT comparator, cross-sensor performance is reasonably good. The EER obtained can be acceptable in convenience applications (2.58%), and the FRR @ FAR=0.01% is of 8.8%, which can be acceptable in high-security applications.

In Table 7, we provide the results of the submission of Halmstad University to the Cross-Eyed 2016 competition, together with the results reported in this paper. At that time, only the SAFE, GABOR, SIFT, LBP, and HOG systems were available. We contributed with three different fusion combinations, named HH1, HH2, and HH3, obtaining the first position in the competition with our HH1 system. A difference in comparison with the present paper is that the LBP and HOG systems of our submissions employed the Euclidean distance (which is the popular choice in the literature with these feature methods, instead of $\chi^2$). It should be also noted that, at the time of submission, the test set had not been released, so our decisions could only be based on the results on the training set. We observed that the SIFT expert already provided error rates close to 0% on the training set (not shown in Table 7). However, it was reasonable to expect a higher error with a bigger dataset, as demonstrated later when the test set was released. Therefore, we contributed to the competition with a fusion of the five systems available (called HH1) to be able to better cope with the generalization issue observable when performance is measured in a bigger set of images. Indeed, in Table 7 it can be seen that performance on the test set is systematically worse than on the training set. Since the combination of the five available systems is computationally heavy in template size (due to the SIFT expert), we also contributed by removing SIFT (combination HH2), and by further removing SAFE (combination HH3), which has a feature extraction time considerably higher than the rest of the systems in our implementation (see Table 3). Thus, our motivation behind HH2 and HH3 was to reduce template size

and feature extraction time. Some differences are observable between our results with the test set and the results reported by the competition [16]. We attribute this to two factors: $i$) the additional 10 subjects included in the test set released, which were not used during the competition, and $ii$) the employment of a different test protocol, since it is not specified by the organizers the exact images used for impostor trials during the competition. Therefore, the experimental framework used in this paper is not exactly the same employed in the Cross-Eyed competition.

Another observation from Tables 5 and 6 is that the best performance is not necessarily obtained by using all available systems. Indeed, the biggest performance improvement occurs after the fusion of two or three systems, with the inclusion of more systems producing smaller improvements (or no improvements at all). The best cross-sensor performance is obtained by fusion of three systems (SIFT, NTNU, and VGG), with EER and FRR reductions of 20-30% in comparison to using SIFT alone. Also, the best combinations for any given number of systems always involve the SIFT expert in any of its versions, either with all key-points, or limiting them to 200. The very good accuracy of the SIFT comparator is not jeopardized by the fusion with other systems that have a performance one or two orders of magnitude worse, but it is complemented to obtain even better cross-sensor error rates. This is because in the trained fusion approach employed, the support of each expert is implicitly weighted by its accuracy. In other simple fusion methods (such as the mean or sum), all experts are considered to have the same weight, independently of its accuracy. This is a common problem of these methods, that makes the worst modalities to yield misleading results more frequently [66, 12].

A careful look at the best combinations of Tables 5 and 6 shows that the NTNU and VGG systems are always chosen first for the fusion. Together with SIFT, these are the three systems with the best individual performance, and they also appear to be very complementary too. Indeed, the best performing combination, as mentioned above, is SIFT+NTNU+VGG. It is also relevant that the combination of two systems only (SIFT+VGG) is also capable of producing top results. However, it should not be taken as a general statement that the best fusion combination always involve the best individual systems. Other fusion rules different than the one employed here may lead

to different results, see for example the experiments around the series of Fingerprint Verification Competitions [67, 68]. This can be also seen by the fact that another combinations in Table 5 (top) have a performance just slightly worse than the best case, but involve systems with a performance two or three times worse than NTNU or VGG. These are for example SIFT+HOG+VGG, or GABOR+SIFT+VGG. At the same time, this demonstrates the power of the fusion approach employed, which is capable of producing top results by fusion of systems with very heterogeneous performance. If we eliminate SIFT from the equation (Table 6), error rates of the best case increase significantly, as mentioned above. Here, the difference in performance between different fusion combinations is much higher, and switching one system with another can have a significant impact. The best cross-sensor FRR is given by HOG+NTNU+VGG, followed closely by HOG+NTNU, but these combinations are not the best when it comes to the EER or to the same-sensor FRR performance. It should be noted that the combinations in Tables 5 and 6 are ranked based on the lowest cross-sensor FRR @ FAR=0.01%, so it might be that another combinations not shown in the tables give better same-sensor performance or better EER. To further investigate this issue, we reran all the possible fusion combinations and looked for the lowest error rate achievable per access type, regardless of the systems involved. Results are shown in Table 8. It can be seen that in the majority of cases, the best result per access type is the one already marked in bold in Table 6. Therefore, the best combinations that optimize the EER or the same-sensor FRR have a poorer cross-sensor FRR performance, and vice-versa. Thus, we need to play by adding or removing different systems depending on the performance metric that we want to give priority to.

## 4. Cross-Sensor Smartphone Periocular Recognition

### *4.1. Database and Protocol*

In the cross-sensor experiments of this section, we use the Visible Spectrum Smartphone Iris (VSSIRIS) database [17], which has images from 28 subjects (56 eyes) captured using the rear camera of two smartphones (Apple iPhone 5S, of 3264×2448 pixels, and Nokia Lumia 1020, of 3072×1728 pixels). They have been obtained in un-

constrained conditions under mixed illumination (natural sunlight and artificial room light, all without flash). Each eye has 5 samples per smartphone, thus 5×56=280 images per device (560 in total). Acquisition is done without flash, in a single session and with semi-cooperative subjects. Figure 6 (bottom) shows some examples.

All images of VSSIRIS are annotated manually, so radius and center of the pupil and sclera circles are available, which are used as input for our experiments. Images are resized via bicubic interpolation to have the same sclera radius (set to $R_s$=145, average radius of the whole database). We use the sclera for normalization since it is not affected by dilation. Then, images are aligned by extracting a square region of $6R_s \times 6R_s$ (871×871) around the sclera center. This size is set empirically to ensure that all available images have sufficient margin to the four sides of the sclera center. Here, there is sufficient availability to the four sides of the eye, so the normalized images have the eye centered in the image, as can be seen in Figure 1 (bottom). Images are further processed by Contrast-Limited Adaptive Histogram Equalization (CLAHE) [60] to compensate variability in local illumination.

We carry out verification experiments, with each eye considered a different user. We compare images both from the same device (*same-sensor*) and from different devices (*cross-sensor*). Genuine trials are obtained by comparing each image of an eye to the remaining images of the same eye, avoiding symmetric comparisons. Impostor trials are done by comparing the $1^{st}$ image of an eye to the $2^{nd}$ image of the remaining eyes. The experimental protocol is summarized in Table 9. The smaller size of VSSIRIS in comparison with the Cross-Eyed database results in the availability of less scores, therefore we have not separated the database into training and test sets.

Parameters of the periocular systems are set as follows. Regarding the SAFE descriptor, the annular band of the first circular ring starts at the sclera circle ($R$=145 pixels), and the band of the last ring ends at the boundary of the image, resulting in a ROI of $871 \times 871$ pixels around the eye center. The availability of sufficient margin around the four sides of the eye makes possible to have a bigger ROI with VSSIRIS, as can be shown in Figure 1, third column. This availability also allows one extra row in the grid employed with GABOR, LBP and HOG experts, having 8×8=64 blocks of 109×109 pixels, although the four blocks of the corners and the four blocks of the image cen-

ter are not considered, effectively resulting in 56 blocks (some more than Cross-Eyed, which has 48 blocks of size 88×88 each). The GABOR operator employs filter wavelengths spanning from 55 to 7 pixels, which are set proportional to the block size as 109/2≈55 to 109/16≈7. Regarding VGG, images are resized to 224×224, which are the input dimensions of this CNN. Table 2 (bottom) indicates the size of the feature vector for a given periocular image with the different experts employed. Experiments have been done in the same machine and with the same algorithm implementations than Cross-Eyed (Section 3.1). Size of stored template files, and the extraction and comparison times are given in Table 3 (bottom).

### *4.2. Results: Individual Systems*

The performance of individual systems is reported in Figure 9 and Table 10. Similarly as Section 3, we adopt as measures of accuracy the Equal Error Rate and the False Rejection Rate (FRR) at a False Acceptance Rate (FAR) of 0.01%. We also provide in Figure 10 the cross-sensor verification accuracy of each system against its template size. Given the small error rates of the SIFT expert in same-sensor comparisons, we report experiments with 200 key-points per image only as well.

By comparing Table 4 and Table 10, it can be observed that same-sensor experiments with the VSSIRIS database usually exhibit smaller error rates for any given comparator. Possible explanations might be that the ROI of VSSIRIS images is bigger (871×871 vs. 613×701), or that the VSSIRIS database has less users (28 vs. 90 subjects). However, to prove these assumptions, additional experiments would be necessary. On the other hand, despite these facts, cross-sensor error rates with VSSIRIS are significantly worse with some comparators (e.g. SIFT, HOG, or NTNU). The difference is specially relevant with the SIFT expert, where cross-sensor error rates on Cross-Eyed (Table 4) were 0.28% (EER) and 0.88% (FRR), but here they increase one order of magnitude here, up to 1.6% (EER) and 12.7% (FRR). This is despite the higher number of SIFT key-points per image with VSSIRIS due to a higher image size (∼3000 vs. ∼1900 on average). It is thus interesting that the comparators employed in this paper are more robust to the variability existing between NIR and VW images (Cross-Eyed database) than the variability between images in the same VW spectrum

captured with two different smartphones (VSSIRIS database). It should be noted that images in Cross-Eyed are obtained with a dual spectrum imaging sensor, which captures NIR and VW images synchronously using a mirror that split the two light beams. Thus, in practice there is no scale, 3D rotation or time lapse difference between corresponding NIR and VW samples. This synchronicity and absence of time span between the images from each spectrum could be one of the reasons of the better cross-sensor performance obtained with the Cross-Eyed database.

Another observation is that same-sensor performance with VSSIRIS is very different depending on the smartphone employed (see Figure 9), even if they involve the same subjects and images are resized to the same size. Contrarily, same-sensor performance with Cross-Eyed tend to be similar regardless of the spectrum employed (Figure 7), which might be explained as well by the synchronicity in the acquisition mentioned above. Previous works have suggested that discrepancy in colors between VW sensors can lead to variability in performance, which is further amplified when images from different sensors are compared. Despite we apply local adaptive contrast equalization, our results suggest that other device-dependant color correction might be of help to compensate variations in performance [27]. It is also relevant with VSSIRIS that performance of the SIFT expert with 200 key-points become comparable (or even worse) than other experts, something that did not happen with Cross-Eyed. This is despite SIFT with 200 key-points still has a template size and a comparison time one or two orders of magnitude bigger than some other systems (Table 3).

Lastly, we analyze the relation between the cross-sensor error rates and the template size. Similarly to the experiments with the Cross-Eyed database, we also observe here an inverse proportion (Figure 10), but with some remarkable exceptions as well. For example, NTNU also shows here top performance despite having a very small template. A positive surprise is given by GABOR and VGG systems. With the Cross-Eyed database, they showed a similar or worse performance than other systems with a smaller template; but here, its performance is significantly better in comparison. On the negative side, we have the variant SIFT-200p. With VSSIRIS, its performance is comparatively worse than other systems, despite having bigger templates. Also, the systems with the smallest template (LBP and HOG) consistently show the worst per-

formance. It is also worth noting that SAFE template size is comparable to LBP and HOG templates, but performance of the latter systems is worse.

### *4.3. Results: Fusion of Periocular Systems*

We now carry out fusion experiments using all the available experts and following the same protocol described in Section 3.3, with results reported in Tables 11 and 12. Due to the smaller size of VSSIRIS, we do not divide the database into training and test set. Instead, the scores of each individual system are mapped to a log-likelihood ratio using the leave-one-subject-out protocol. The set of scores of a given system is divided into 56 folds, leaving out the scores of one user each time. For each fold, the normalization parameters are obtained. Then, the median of the normalization parameters of all folds are computed, which are used to normalize the scores.

Similarly as Cross-Eyed, cross-sensor performance is improved significantly by fusion when the SIFT expert is involved. Here, the relative EER and FRR improvement is bigger, being of 38% and of 73% respectively. This is high in comparison with the reductions observed with Cross-Eyed, which were in the order of 20-30%. On the other hand, absolute performance values with VSSIRIS are worse than with Cross-Eyed, in line with the observations made in the previous section. The best cross-sensor EER with Cross-Eyed achievable by fusion was of 0.22%, but here with VSSIRIS it is of 1%. Similarly, the cross-sensor FRR compares badly (0.62% vs. 3.4%). Also here the SIFT features contribute decisively to a much smaller error rates, as observed by the results when it is limited to 200 key-points, or directly removed from the fusion (bottom part of Table 12). Still, cross-sensor performance is acceptable in the latter case, with an EER of 3.7%, and a FRR @ FAR=0.01% of 10.8%.

Also here, the biggest performance improvement mostly occurs after the fusion of two or three systems. By analyzing the systems involved in the best fusion cases, Table 11 (top) shows that the combination SIFT+NTNU+VGG (which was the winner with Cross-Eyed) produces top results in cross-sensor experiments with VSSIRIS as well. A further look at Tables 11 and 12 also shows that, together with SIFT, NTNU and VGG are always chosen first for the fusion. Again, this is despite the worse performance of these two systems in comparison with SIFT. If we eliminate SIFT (Table 12),

error rates increase, as expected. But with the VSSIRIS database, there is more consistency in the sense than the combinations that optimize the FRR also show top results in the EER, and vice-versa. We re-ran again all the possible fusion combinations and looked for the lowest error rate achievable per access type, regardless of the systems involved, with results given in Table 13. As it can be observed, the cases marked in bold in Table 12 are close to best attainable performance per access type. Therefore, a single combination is good to optimize both EER and FRR. A good particular one is given by just two experts (NTNU+VGG), which produces nearly the best achievable EERs, and also has FRR accuracies close to the best possible results.

## 5. Conclusion

Periocular biometrics has rapidly evolved to competing with face or iris recognition [1]. The periocular region has shown to be as discriminative as the full face, with the advantage that it is more tolerant to variability in expression, blur/downsampling [69], or occlusions [70, 18]. Under difficult conditions, such as acquisition portals, [71, 72, 73], distant acquisition, [74, 75], smartphones, [27], webcams, or digital cameras, [20, 63], the periocular modality is also shown to be clearly superior to the iris modality, mostly due to the small size of the iris or the use of visible illumination.

As biometric technologies are extensively deployed, it will be common to compare data captured with different sensors, or from uncontrolled non-homogeneous environments. Unfortunately, comparison of heterogeneous biometric data for recognition purposes is known to decrease performance significantly [8]. Hence, as new practical applications evolve, new challenges arise, as well the need for developing new algorithms to address them. In this context, we address in this paper the problem of biometric sensor interoperability, with recognition by periocular images as test-bed.

Inspired by the $1^{st}$ Cross-Spectral Iris/Periocular Competition (Cross-Eyed) [16], we propose a multialgorithm fusion strategy at the score level which combines up to seven different periocular algorithms. The aim of this competition was to evaluate periocular recognition algorithms when images from visible and near-infrared images are compared. Following a probabilistic approach, output scores of each individual system

are mapped to log-likelihood ratios by linear logistic regression. Under independence assumptions (as with the use of different features), the sum of log-likelihood ratios results in another log-likelihood ratio [25], therefore providing a simple, yet an elegant approach to fuse different systems by simply summing the score given by each system. This approach has been applied previously to cross-sensor comparison of face or fingerprint modalities [15] as well, providing also excellent results in other competition benchmarks involving these modalities [26]. We employ in this paper three different systems based on the most widely used features in periocular research [18], as well as three in-house algorithms that we proposed recently [19, 20, 21], and one system based on Convolutional Neural Networks [22]. The proposed approach was submitted to the mentioned Cross-Eyed evaluation, which ranked first in the evaluation. The paper is complemented with cross-sensor periocular experiments in the same spectrum as well. For this purpose, we use the Visible Spectrum Smartphone Iris database (VSSIRIS) [17], which contains images in visible range from two different smartphones.

We first analyze the individual systems employed not only from the point of view of its cross-sensor performance, but also from its template size and computation times. We observe that the expert having the biggest template size and computation time is the most accurate in terms of individual performance, also contributing decisively to the fusion. In the experiments reported in this paper, significant improvements in performance are obtained with the proposed fusion approach, leading to an EER of 0.22% in visible to near-infrared cross-sensor comparisons, and 1% in cross-sensor comparison of smartphone images. The FRR in high-security environments (at FAR=0.01%) is also very good, being of 0.62% and 3.4% respectively. If the most computational expensive system is removed for storage- and time-saving purposes, recognition errors increase by one order of magnitude, although the results are also acceptable.

Interestingly, the best performance is not obtained necessarily by combination of all the available experts; instead, the best results are obtained by fusion of just two or three systems, similar to other related studies in biometrics [68]. It is also worth noting that the systems producing the best fusion performance have a individual performance that differs in one or two orders of magnitude. In the probabilistic approach employed, each expert is implicitly weighed by its individual accuracy, so the most reliable modalities

will have a dominant role [76]. It is therefore a very efficient method to cope with systems having heterogeneous performance. On the contrary, in conventional score-level fusion approaches (like the mean or sum), each system is given the same weight regardless of its accuracy, a common drawback that makes the worst experts to produce misleading results more frequently [66]. Another relevant observation is that cross-sensor error rates are higher with the database captured in the same spectrum (VSSIRIS) than the database which contains images in different spectra (Cross-Eyed). This is an interesting phenomena, since one would expect that the comparison of images captured with visible cameras would produce better results (even if the cameras are different) than the comparison of near-infrared and visible images. Some authors point out that the discrepancy in colors between sensors in visible range can be very important, leading to a significant decrease in performance when images from these sensors are compared without applying appropriate device-dependant color corrections [27].

As future work, we are exploring to exploit deep learning frameworks to learn the variability between images in different spectra, or captured with different sensors. One plausible approach is the use of Generative Adversarial Networks [77] to produce samples from one spectrum to the other. This has the advantage that images can be compared using standard feature descriptors such as the ones employed in this paper, which have been shown to work better if images are from the same spectrum.

In the context of smartphone recognition, where high resolution images are usual, fusion with the iris modality is another possibility to increase recognition accuracy [63]. However, it demands segmentation, which might be an issue if the image quality is not sufficiently high [7], which also motivates pursuing the periocular modality, as in the current study. We will also validate our methodology using databases not only limited to two devices or spectra, e.g. [27, 40], and also including more extreme variations in camera specifications and imaging conditions, such as low resolution, lightning or pose variability. For such low quality imaging conditions, super-resolution techniques may be also helpful [78], and will be investigated as well.

**Acknowledgment**

Part of this work was done while F. A.-F. was a visiting researcher at the Norwegian University of Science and Technology in Gjøvik (Norway), funded by EU COST Action IC1106. Authors from HH thank the Swedish Research Council, the Swedish Knowledge Foundation, and the Swedish Innovation Agency VINNOVA for funding his research. Authors from UAM are funded by the Spanish MINECO/FEDER through the CogniMetrics Project (Grant TEC2015-70627-R).

**References**

[1] F. Alonso-Fernandez, J. Bigun, A survey on periocular biometrics research, Pattern Recognition Letters 82 (2016) 92–105.

[2] H. Proenca, M. Nixon, M. Nappi, E. Ghaleb, G. Ozbulak, H. Gao, H. K. Ekenel, K. Grm, V. Struc, H. Shi, X. Zhu, S. Liao, Z. Lei, S. Z. Li, W. Gutfeter, A. Pacut, J. Brogan, W. J. Scheirer, E. Gonzalez-Sosa, R. Vera-Rodriguez, J. Fierrez, J. Ortega-Garcia, D. Riccio, L. D. Maio, Trends and controversies, IEEE Intelligent Systems 33 (3) (2018) 41–67. doi:https://doi.org/10.1109/MIS.2018.033001416.

[3] E. Gonzalez-Sosa, J. Fierrez, R. Vera-Rodriguez, F. Alonso-Fernandez, Facial soft biometrics for recognition in the wild: Recent works, annotation and cots evaluation, IEEE Trans. on Information Forensics and Security 13 (8) (2018) 2001–2014. doi:https://doi.org/10.1109/TIFS.2018.2807791.

[4] R. R. Jillela, A. Ross, V. N. Boddeti, B. V. K. V. Kumar, X. Hu, R. Plemmons, P. Pauca, Handbook of Iris Recognition, Springer, 2013, Ch. Iris segmentation for challenging periocular images, pp. 281–308.

[5] I. Nigam, M. Vatsa, R. Singh, Ocular biometrics: A survey of modalities and fusion approaches, Information Fusion 26 (0) (2015) 1 – 35.

[6] A. K. Jain, A. Kumar, Second Generation Biometrics, Springer, 2011, Ch. Biometrics of next generation: An overview.

[7] F. Alonso-Fernandez, J. Fierrez, J. Ortega-Garcia, Quality measures in biometric systems, IEEE Security and Privacy 10 (6) (2012) 52–62.

[8] A. Jain, K. Nandakumar, A. Ross, 50 years of biometric research: Accomplishments, challenges, and opportunities, Pattern Recognition Letters 79 (2016) 80–105.

[9] M. Moreno-Moreno, J. Fierrez, J. Ortega-Garcia, Biometrics beyond the visible spectrum: Imaging technologies and applications, in: J. Fierrez, J. Ortega-Garcia, A. Esposito, A. Drygajlo, M. Faundez-Zanuy (Eds.), Proceedings of BioID-Multicomm, Vol. 5707 of LNCS, Springer, 2009, pp. 154–161.

[10] R. R. Jillela, A. Ross, Matching face against iris images using periocular information, Proc Intl Conf Image Processing, ICIP.

[11] P. Tome, R. Vera-Rodriguez, J. Fierrez, J. Ortega-Garcia, Facial soft biometric features for forensic face recognition, Forensic Science International 257 (2015) 171–284. doi:http://dx.doi.org/10.1016/j.forsciint.2015.09.002.

[12] J. Fierrez, A. Morales, R. Vera-Rodriguez, D. Camacho, Multiple classifiers in biometrics. part 1: Fundamentals and review, Information Fusion 44 (2018) 57–64.

[13] A. Lumini, L. Nanni, Overview of the combination of biometric matchers, Information Fusion 33 (2017) 71 – 85. doi:https://doi.org/10.1016/j.inffus.2016.05.003.

[14] A. Ross, P. Flynn, A. Jain (Eds.), Handbook of Multibiometrics, Springer, 2006.

[15] F. Alonso-Fernandez, J. Fierrez, D. Ramos, J. Gonzalez-Rodriguez, Quality-based conditional processing in multi-biometrics: Application to sensor interoperability, IEEE Trans. on Systems, Man and Cybernetics-Part A: Systems and Humans 40 (6) (2010) 1168–1179.

[16] A. F. Sequeira, L. Chen, J. Ferryman, F. Alonso-Fernandez, J. Bigun, K. B. Raja, R. Raghavendra, C. Busch, P. Wild, Cross-eyed - cross-spectral iris/periocular recognition database and competition, Proc Intl Conf of the Biometrics Special Interest Group, BIOSIG.

[17] K. B. Raja, R. Raghavendra, V. K. Vemuri, C. Busch, Smartphone based visible iris recognition using deep sparse filtering, Pattern Recognition Letters 57 (2015) 33–42.

[18] U. Park, R. R. Jillela, A. Ross, A. K. Jain, Periocular biometrics in the visible spectrum, IEEE Trans Information Forensics and Security 6 (1) (2011) 96–106.

[19] F. Alonso-Fernandez, A. Mikaelyan, J. Bigun, Compact multi-scale periocular recognition using SAFE features, Proc Intl Conf Pattern Recognition, ICPR.

[20] F. Alonso-Fernandez, J. Bigun, Near-infrared and visible-light periocular recognition with gabor features using frequency-adaptive automatic eye detection, IET Biometrics 4 (2) (2015) 74–89.

[21] K. B. Raja, R. Raghavendra, C. Busch, Scale-level score fusion of steered pyramid features for cross-spectral periocular verification, in: 2017 20th International Conference on Information Fusion (Fusion), 2017, pp. 1–7. doi:10.23919/ICIF.2017.8009721.

[22] O. M. Parkhi, A. Vedaldi, A. Zisserman, Deep face recognition, Proc British Machine Vision Conference, BMVC.

[23] S. Pigeon, P. Druyts, P. Verlinde, Applying logistic regression to the fusion of the NIST'99 1-speaker submissions, Digital Signal Processing 10 (2000) 237–248.

[24] N. Brummer, L. Burget, J. Cernocky, O. Glembek, F. Grezl, M. Karafiat, D. van Leeuwen, P. Matejka, P. Scwartz, A. Strasheim, Fusion of heterogeneous speaker recognition systems in the STBU submission for the NIST Speaker Recognition Evaluation 2006, IEEE Trans. on Audio, Speech and Signal Processing 15 (7) (2007) 2072–2084.

[25] R. Duda, P. Hart, D. Stork, Pattern Classification - 2nd Edition, 2004.

[26] N. Poh, T. Bourlai, J. Kittler, L. Allano, F. Alonso-Fernandez, O. Ambekar, J. Baker, B. Dorizzi, O. Fatukasi, J. Fierrez, H. Ganster, J. Ortega-Garcia, D. Maurer, A. Salah, T. Scheidat, C. Vielhauer, Benchmarking quality-dependent and cost-sensitive score-level multimodal biometric fusion algorithms, IEEE Trans. on Information Forensics and Security 4 (4) (2009) 849 – 866.

[27] G. Santos, E. Grancho, M. V. Bernardo, P. T. Fiadeiro, Fusing iris and periocular information for cross-sensor recognition, Pattern Recognition Letters 57 (2015) 52–59.

[28] K. B. Raja, R. Raghavendra, C. Busch, Dynamic scale selected laplacian decomposed frequency response for cross-smartphone periocular verification in visible spectrum, in: Proc 19th International Conference on Information Fusion (FUSION), 2016, pp. 2206–2212.

[29] C. Kandaswamy, J. C. Monteiro, L. M. Silva, J. S. Cardoso, Multi-source deep transfer learning for cross-sensor biometrics, Neural Computing and Applications 28 (9) (2017) 2461–2475. doi:10.1007/s00521-016-2325-5.

[30] M. D. Marsico, C. Galdi, M. Nappi, D. Riccio, FIRME: Face and iris recognition for mobile engagement, Image and Vision Computing 32 (12) (2014) 1161 – 1172. doi:https://doi.org/10.1016/j.imavis.2013.12.014.

[31] L. Xiao, Z. Sun, T. Tan, Fusion of iris and periocular biometrics for cross-sensor identification, Proc. 7th Chinese Conference on Biometric Recognition, CCBR (2012) 202–209.

[32] A. Sharma, S. Verma, M. Vatsa, R. Singh, On cross spectral periocular recognition, Proc Intl Conf Image Processing, ICIP.

[33] A. Bosch, A. Zisserman, X. Munoz, Representing shape with a spatial pyramid kernel, Proc. of the 6th ACM International Conference on Image and Video Retrieval, CIVR (2007) 401–408.

[34] N. P. Ramaiah, A. Kumar, On matching cross-spectral periocular images for accurate biometrics identification, in: Proc IEEE 8th International Conference on Biometrics Theory, Applications and Systems (BTAS), 2016, pp. 1–6. doi:10.1109/BTAS.2016.7791190.

[35] S. S. Behera, M. Gour, V. Kanhangad, N. Puhan, Periocular recognition in cross-spectral scenario, in: Proc IEEE International Joint Conference on Biometrics, IJCB, 2017, pp. 681–687. doi:10.1109/BTAS.2017.8272757.

[36] Z. Cao, N. A. Schmid, Fusion of operators for heterogeneous periocular recognition at varying ranges, Pattern Recognition Letters 82, Part 2 (2016) 170 – 180.

[37] J. Chen, S. Shan, C. He, G. Zhao, M. Pietikainen, X. Chen, W. Gao, Wld: A robust local image descriptor, IEEE Transactions on Pattern Analysis and Machine Intelligence 32 (9) (2010) 1705–1720.

[38] T. Ojala, M. Pietikainen, T. Maenpaa, Multiresolution gray-scale and rotation invariant texture classification with local binary patterns, IEEE Trans. on Pattern Analysis and Machine Intelligence 24 (7) (2002) 971–987.

[39] N. Dalal, B. Triggs, Histograms of oriented gradients for human detection, Proc Intl Conf Computer Vision and Pattern Recogn, CVPR.

[40] N. Vetrekar, K. B. Raja, R. Ramachandra, R. Gad, C. Busch, Multi-spectral imaging for robust ocular biometrics, in: 2018 International Conference on Biometrics (ICB), 2018, pp. 195–201. doi:10.1109/ICB2018.2018.00038.

[41] D. Lowe, Distinctive image features from scale-invariant key points, Intl Journal of Computer Vision 60 (2) (2004) 91–110.

[42] J. Bigun, Vision with Direction, Springer, 2006.

[43] F. Smeraldi, J. Bigün, Retinal vision applied to facial features detection and face authentication, Pattern Recognition Letters 23 (4) (2002) 463–475.

[44] M. Unser, N. Chenouard, D. V. D. Ville, Steerable pyramids and tight wavelet frames in l2(bbrd), IEEE Trans. Image Processing 20 (2011) 2705–2721.

[45] M. N. Do, M. Vetterli, Rotation invariant texture characterization and retrieval using steerable wavelet-domain hidden markov models, IEEE Transactions on Multimedia 4 (4) (2002) 517–527.

[46] G. Tzagkarakis, B. Beferull-Lozano, P. Tsakalides, Rotation-invariant texture retrieval with gaussianized steerable pyramids, IEEE Transactions on Image Processing 15 (9) (2006) 2702–2718.

[47] J. Portilla, E. P. Simoncelli, A parametric texture model based on joint statistics of complex wavelet coefficients, International journal of computer vision 40 (1) (2000) 49–70.

[48] S. Lyu, E. P. Simoncelli, Modeling multiscale subbands of photographic images with fields of gaussian scale mixtures, IEEE Transactions on pattern analysis and machine intelligence 31 (4) (2009) 693–706.

[49] S.-T. Li, Y. Li, Y.-N. Wang, Comparison and fusion of multiresolution features for texture classification, in: Machine Learning and Cybernetics, 2004. Proceedings of 2004 International Conference on, Vol. 6, IEEE, 2004, pp. 3684–3688.

[50] M. El Aroussi, M. El Hassouni, S. Ghouzali, M. Rziza, D. Aboutajdine, Novel face recognition approach based on steerable pyramid feature extraction, in: Image Processing (ICIP), 2009 16th IEEE International Conference on, IEEE, 2009, pp. 4165–4168.

[51] C. Su, Y. Zhuang, L. Huang, F. Wu, Steerable pyramid-based face hallucination, Pattern Recognition 38 (6) (2005) 813–824.

[52] E. P. Simoncelli, W. T. Freeman, The steerable pyramid: A flexible architecture for multi-scale derivative computation, in: Image Processing, 1995. Proceedings., International Conference on, Vol. 3, IEEE, 1995, pp. 444–447.

[53] W. T. Freeman, E. H. Adelson, et al., The design and use of steerable filters, IEEE Transactions on Pattern analysis and machine intelligence 13 (9) (1991) 891–906.

[54] H. Greenspan, S. Belongie, R. Goodman, P. Perona, Rotation invariant texture recognition using a steerable pyramid, in: Pattern Recognition, 1994. Vol. 2-Conference B: Computer Vision & Image Processing., Proceedings of the 12th IAPR International. Conference on, Vol. 2, IEEE, 1994, pp. 162–167.

[55] V. Ojansivu, J. Heikkilä, Blur insensitive texture classification using local phase quantization, in: Image and signal processing, Springer, 2008, pp. 236–243.

[56] F. Alonso-Fernandez, P. Tome-Gonzalez, V. Ruiz-Albacete, J. Ortega-Garcia, Iris recognition based on SIFT features, Proc IEEE Intl Conf Biometrics, Identity and Security, BIDS.

[57] G. B. Huang, M. Ramesh, T. Berg, E. Learned-Miller, Labeled faces in the wild: A database for studying face recognition in unconstrained environments, Tech. Rep. 07-49, University of Massachusetts, Amherst (October 2007).

[58] L. Wolf, T. Hassner, I. Maoz, Face recognition in unconstrained videos with matched background similarity, in: Proc. Conf on Computer Vision and Pattern Recognition, CVPR, 2011, pp. 529–534.

[59] K. Hernandez-Diaz, F. Alonso-Fernandez, J. Bigun, Periocular recognition using CNN features off-the-shelf, in: Proc International Conference of the Biometrics Special Interest Group (BIOSIG), 2018, pp. 1–5. doi:10.23919/BIOSIG.2018.8553348.

[60] K. Zuiderveld, Graphics Gems IV (1994) 474–485.

[61] C. Rathgeb, A. Uhl, Secure iris recognition based on local intensity variations, Proc ICIAR 6112 (2010) 266–275.

[62] C. Padole, H. Proenca, Periocular recognition: Analysis of performance degradation factors, Proc Intl Conf Biometrics, ICB (2012) 439–445.

[63] F. Alonso-Fernandez, A. Mikaelyan, J. Bigun, Comparison and fusion of multiple iris and periocular matchers using near-infrared and visible images, Proc Intl Workshop Biometrics and Forensics, IWBF.

[64] K. Hollingsworth, S. S. Darnell, P. E. Miller, D. L. Woodard, K. W. Bowyer, P. J. Flynn, Human and machine performance on periocular biometrics under near-infrared light and visible light, IEEE Trans Information Forensics and Security 7 (2) (2012) 588–601.

[65] D. L. Woodard, S. J. Pundlik, J. R. Lyle, P. E. Miller, Periocular region appearance cues for biometric identification, Proc IEEE Computer Vision and Pattern Recognition Biometrics Workshop, CVPRW.

[66] A. Jain, K. Nandakumar, A. Ross, Score normalization in multimodal biometric systems, Pattern Recognition 38 (12) (2005) 2270–2285.

[67] J. Fierrez-Aguilar, Y. Chen, J. Ortega-Garcia, A. Jain, Incorporating image quality in multi-algorithm fingerprint verification, Proc Intl Conf Biometrics, ICB Springer LNCS-3832 (2006) 213–220.

[68] J. Fierrez-Aguilar, L. Nanni, J. Ortega-Garcia, R. Capelli, D. Maltoni, Combining Multiple Matchers for Fingerprint Verification: A Case Study in FVC2004, Proc Int Conf Image Analysis and Processing, ICIAP Springer LNCS-3617 (2005) 1035–1042.

[69] P. E. Miller, J. R. Lyle, S. J. Pundlik, D. L. Woodard, Performance evaluation of local appearance based periocular recognition, Proc IEEE Int. Conf Biometrics: Theory, Applications, and Systems, BTAS.

[70] F. Juefei-Xu, M. Savvides, Subspace-based discrete transform encoded local binary patterns representations for robust periocular matching on NIST face recognition grand challenge, IEEE Trans Image Processing 23 (8) (2014) 3490–3505.

[71] D. Woodard, S. Pundlik, P. Miller, R. Jillela, A. Ross, On the fusion of periocular and iris biometrics in non-ideal imagery, Proc IAPR Intl Conf Pattern Recognition, ICPR.

[72] V. Boddeti, J. Smereka, B. Kumar, A comparative evaluation of iris and ocular recognition methods on challenging ocular images, Proc Intl Joint Conf Biometrics, IJCB (2011) 1–8.

[73] A. Ross, R. Jillela, J. Smereka, V. Boddeti, B. Kumar, R. Barnard, X. Hu, P. Pauca, R. Plemmons, Matching highly non-ideal ocular images: An information fusion approach, Proc Intl Conf Biometrics, ICB (2012) 446–453.

[74] C.-W. Tan, A. Kumar, Human identification from at-a-distance images by simultaneously exploiting iris and periocular features, Proc Intl Conf Pattern Recognition, ICPR (2012) 553–556.

[75] P. Tome, J. Fierrez, R. Vera-Rodriguez, M. Nixon, Soft biometrics and their application in person recognition at a distance, IEEE Transactions on Information Forensics and Security 9 (3) (2014) 464–475. doi:http://dx.doi.org/10.1109/TIFS.2014.2299975.

[76] J. Fierrez-Aguilar, J. Ortega-Garcia, J. Gonzalez-Rodriguez, J. Bigun, Discriminative Multimodal Biometric Authentication Based on Quality Measures, Pattern Recognition 38 (5) (2005) 777–779.

[77] I. Goodfellow, J. Pouget-Abadie, M. Mirza, B. Xu, D. Warde-Farley, S. Ozair, A. Courville, Y. Bengio, Generative adversarial nets, in: Z. Ghahramani, M. Welling, C. Cortes, N. D. Lawrence, K. Q. Weinberger (Eds.), Advances in Neural Information Processing Systems 27, Curran Associates, Inc., 2014, pp. 2672–2680.

[78] F. Alonso-Fernandez, R. A. Farrugia, J. Bigun, J. Fierrez, E. Gonzalez-Sosa, A survey of super-resolution in iris biometrics with evaluation of dictionary-learning, IEEE Access 7 (2019) 6519–6544. doi:10.1109/ACCESS.2018.2889395.

**List of Figures**

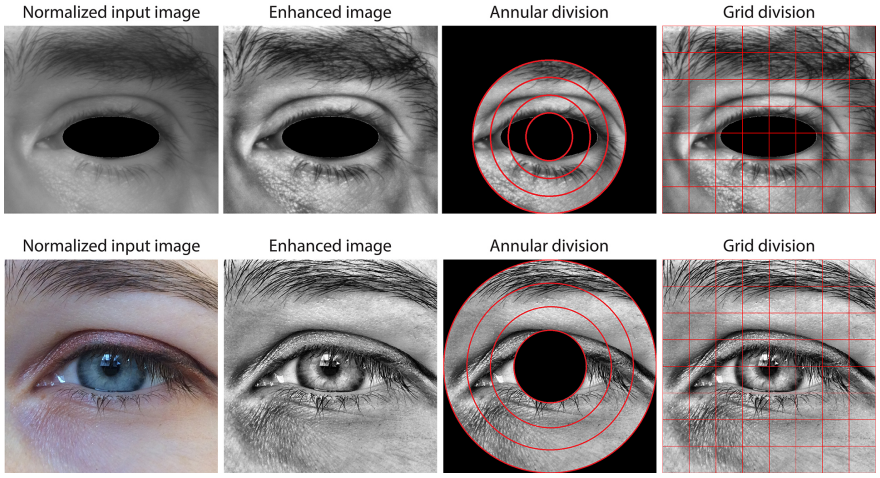


Figure 1: Example images from Cross-Eyed (top row) and VSSIRIS (bottom row) database. First column: input image. Second: after applying CLAHE (see Sect. 3.1). Third and fourth: ROI of the different systems (see Sect. 2).

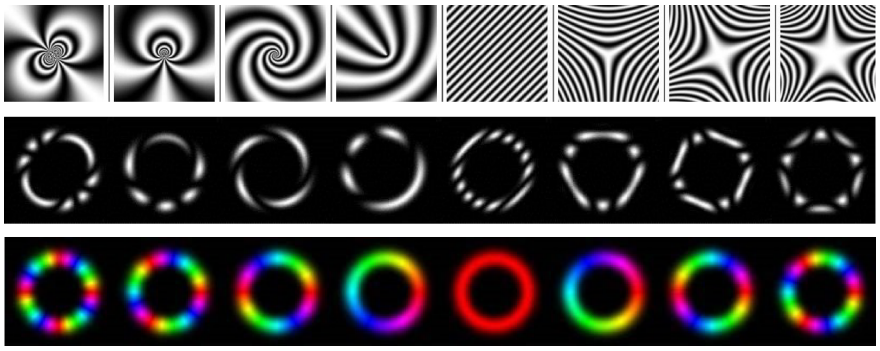

Figure 2: *Top*: Sample patterns of the family of harmonic functions used as basis of the SAFE expert. *Middle*: One pattern per original (top) but in selected ring support. *Bottom*: Complex filters used to detect patterns above. Hue in color images encode the direction, and saturation represents the complex magnitude.

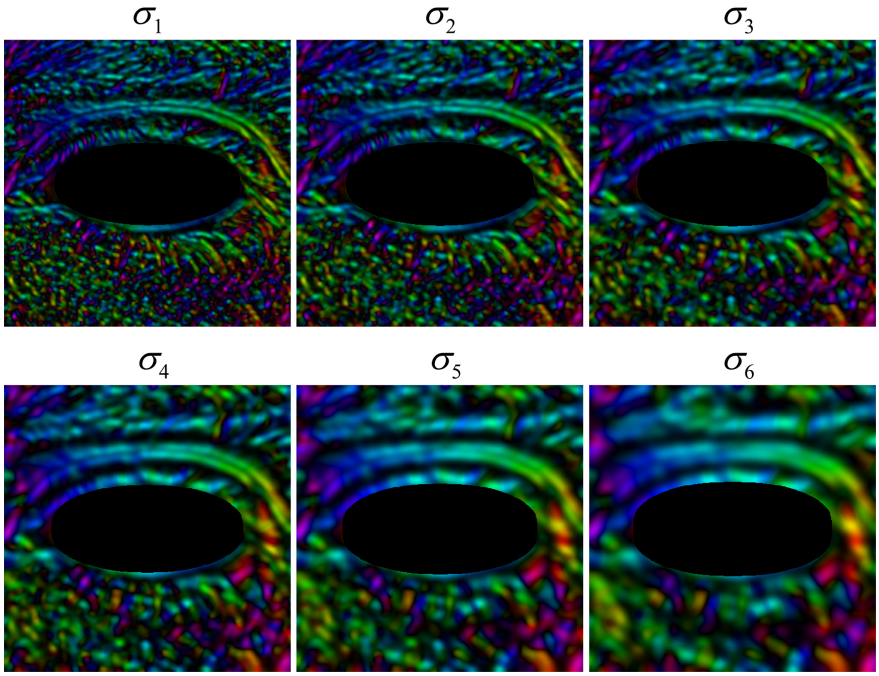


Figure 3: Orientation map at different scales of the input image shown in Figure 1 (top row).

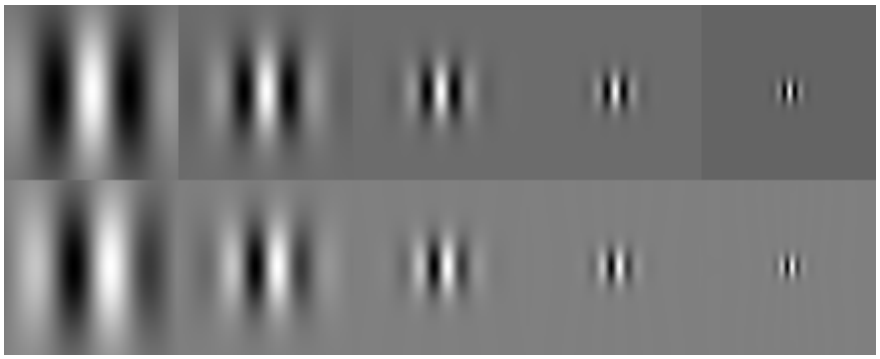

Figure 4: Gabor filters with vertical orientation (top: real part, bottom: imaginary part). Depicted filters are of size $88 \times 88$, with wavelengths spanning logarithmically the range from 44 (first column) to 6 pixels (last column).

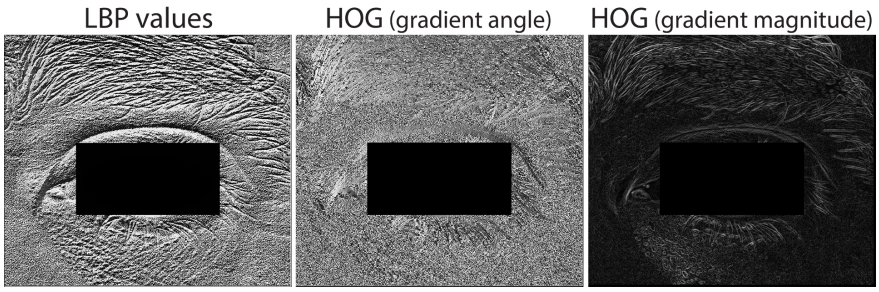


Figure 5: Example of LBP and HOG features of the input image shown in Figure 1 (top row).

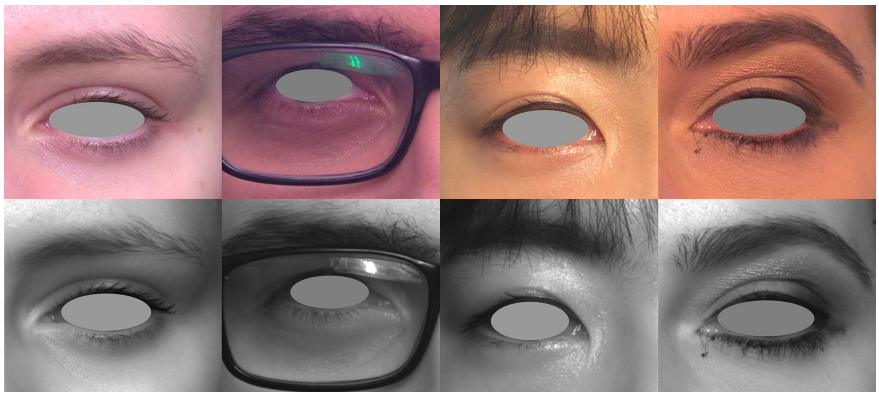

(a) Cross-Eyed database (top row: visible images, bottom: near-infrared)

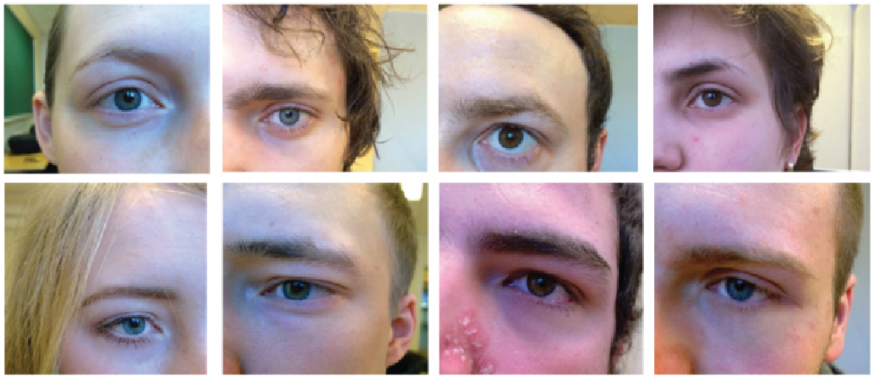

(b) VSSIRIS database (top row: Apple iPhone 5S, bottom: Nokia Lumia 1020; images taken from [17])

Figure 6: Sample periocular images.

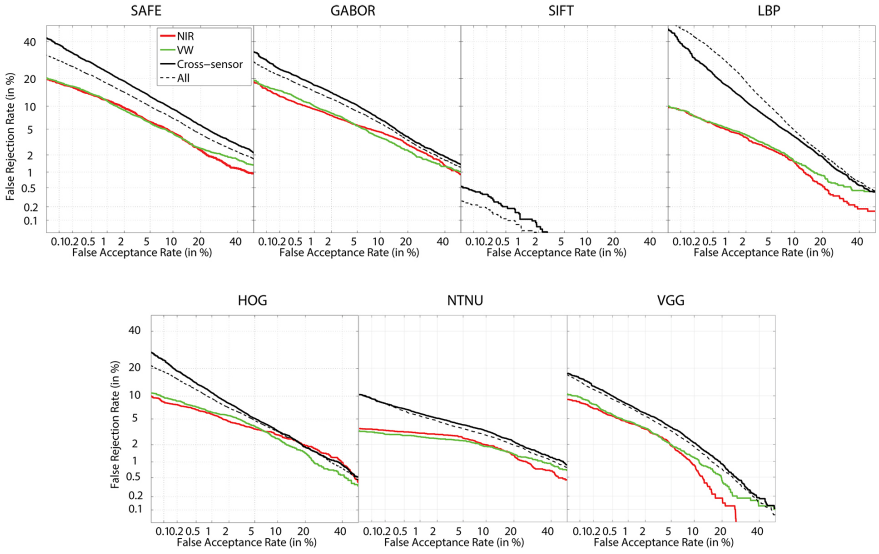


Figure 7: Cross-Eyed database, test set: Verification results of the individual systems. Best seen in color.

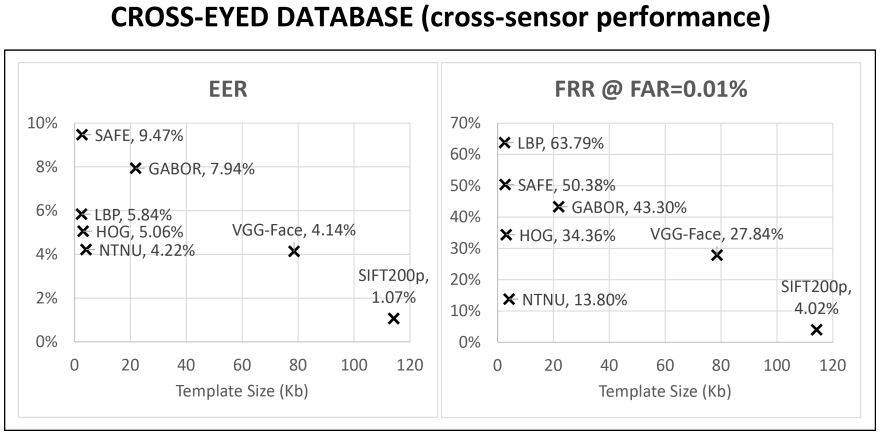


Figure 8: Cross-Eyed database, test set: Cross-sensor performance of the individual systems vs. template size.

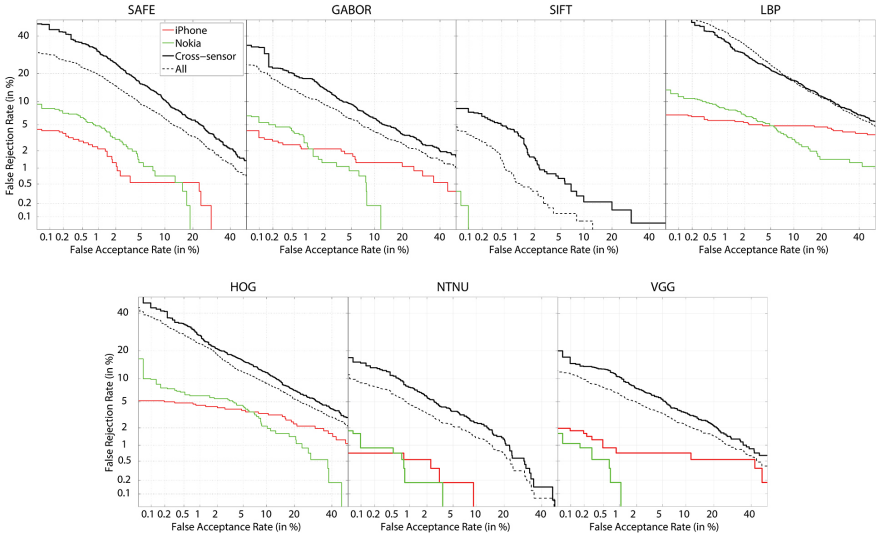


Figure 9: VSSIRIS database: Verification results of the individual systems. Best seen in color.

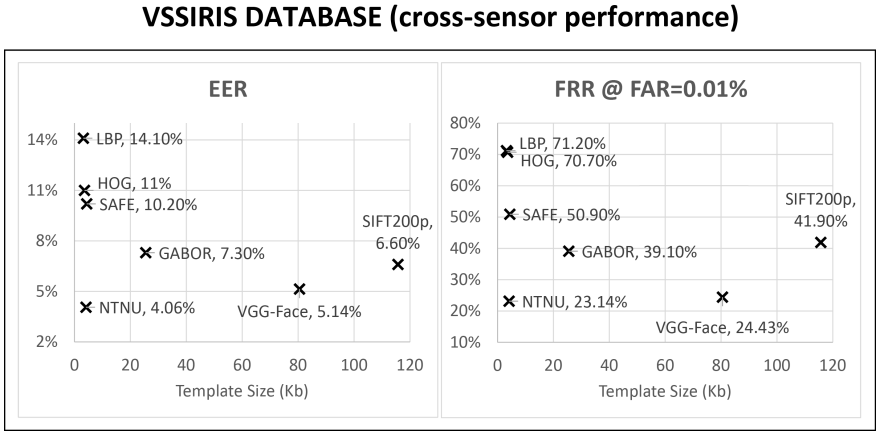


Figure 10: VSSIRIS database, test set: Cross-sensor performance of the individual systems vs. template size.

**List of Tables**

| Cross-Eyed database | | | |
|---|---|---|---|
| **Comparison type** | | **Training** (30 subjects) | **Test** (90 subjects) |
| Same-sensor | Genuine | 30 × 2 eyes × (7+6+...+1) = 1,680 | 90 × 2 eyes × (7+6+...+1) = 5,040 |
| | Impostor | 30 × 29 × (4 left + 4 right) = 6,960 | 90 × 89 × (2 left + 2 right) = 32,040 |
| Cross-sensor | Genuine | 30 × 2 eyes × 8 left × 8 right = 3,840 | 90 × 2 eyes × 8 left × 8 right =11,520 |
| | Impostor | 30 × 29 × (4 left + 4 right) × 2 sensors = 13,920 | 90 × 89 × (2 left + 2 right) × 2 sensors = 64,080 |

Table 1: Cross-Eyed database: Experimental protocol.

**Cross-Eyed database**

| system | size | data type |
|---|---|---|
| SAFE | 6×3×9=162 | complex number |
| GABOR | 48×30=1440 | real number |
| SIFT | 128 per key point | real number |
| LBP, HOG | 48×8=384 | real number |
| NTNU | 9472 | integer number |
| VGG | 100352 | real number |

**VSSIRIS database**

| system | size | data type |
|---|---|---|
| SAFE | 6×3×9=162 | complex number |
| GABOR | 56×30=1680 | real number |
| SIFT | 128 per key point | real number |
| LBP, HOG | 56×8=448 | real number |
| NTNU | 9472 | integer number |
| VGG | 100352 | real number |

Table 2: Size of the feature vector for each comparator.

**Cross-Eyed database**

| system | Template Size | Extraction Time | Comparison Time |
|---|---|---|---|
| SAFE | 2.71 Kb | 2.98 sec | 0.2 ms |
| GABOR | 21.89 Kb | 0.49 sec | 0.3 ms |
| SIFT | 1020 Kb | 0.94 sec | 0.58 s |
| SIFT-200p | 114.2 Kb | - | 6.9 ms |
| LBP | 2.53 Kb | 0.16 sec | <0.1 ms |
| HOG | 3.11 Kb | 0.01 sec | <0.1 ms |
| NTNU | 4.15 Kb | 0.6 sec | 0.7 ms |
| VGG | 78.54 Kb | 0.37 sec | 1.28 ms |

**VSSIRIS database**

| system | Template Size | Extraction Time | Comparison Time |
|---|---|---|---|
| SAFE | 4.4 Kb | 11.86 sec | <0.1 ms |
| GABOR | 25.5 Kb | 0.53 sec | 0.3 ms |
| SIFT | 2138 Kb | 1.5 sec | 1.1 s |
| SIFT-200p | 115.7 Kb | - | 6.1 ms |
| LBP | 3.2 Kb | 0.17 sec | <0.1 ms |
| HOG | 3.6 Kb | 0.13 sec | <0.1 ms |
| NTNU | 4.14 Kb | 0.56 sec | 0.7 ms |
| VGG | 80.5 Kb | 0.59 sec | 1.49 ms |

Table 3: Size of the template file and computation times.

| | Equal Error Rate (EER) | | | | FRR @ FAR=0.01% | | | |
|---|---|---|---|---|---|---|---|---|
| | Same sensor | | | | Same sensor | | | |
| **system** | **NIR** | **VW** | **cross-sensor** | **all** | **NIR** | **VW** | **cross-sensor** | **all** |
| SAFE | 5.85% | 5.67% | 9.47% (+67%) | 8.01% | 22.4% | 24.23% | 50.38% (+124.9%) | 37.89% |
| GABOR | 5.48% | 5.34% | 7.94% (+48.7%) | 7.28% | 26.25% | 23.68% | 43.3% (+82.9%) | 35.54% |
| SIFT | 0.02% | 0% | 0.28% (+Inf) | 0.19% | 0.02% | 0% | 0.88% (+Inf) | 0.48% |
| SIFT-200p | 0.15% | 0.31% | 1.07% (+613.3%) | 0.81% | 0.44% | 0.76% | 4.02% (+813.6%) | 2.57% |
| LBP | 3.03% | 3.27% | 5.84% (+92.7%) | 7.02% | 10.97% | 12.86% | 63.79% (+481.5%) | 57.46% |
| HOG | 3.84% | 4.19% | 5.06% (+31.8%) | 4.84% | 11.76% | 14.93% | 34.36% (+192.2%) | 30.05% |
| NTNU | 2.83% | 2.45% | 4.22% (+72.2%) | 3.82% | 3.93% | 3.57% | 13.8% (+286.6%) | 13.57% |
| VGG | 2.91% | 2.92% | 4.14% (+42.3%) | 3.85% | 10.81% | 13.26% | 27.84% (+157.5%) | 22.85% |

Table 4: Cross-Eyed database, test set: Verification results of the individual systems. The relative variation of cross-sensor performance with respect to the best same-sensor performance is given in brackets.

**USING ALL THE SYSTEMS AVAILABLE**

| # | systems: safe | gabor | sift | lbp | hog | ntnu | vgg | Equal Error Rate (EER): NIR | VW | cross-sensor | all | FRR @ FAR=0.01%: NIR | VW | cross-sensor | all |
|---|---|---|---|---|---|---|---|---|---|---|---|---|---|---|---|
| 1 | | | x | | | | | **0.02** (+0%) | **0** (+0%) | 0.28 (+0%) | 0.19 (+0%) | **0.02** (+0%) | **0** (+0%) | 0.88 (+0%) | 0.48 (+0%) |
| | | | | | | x | | 2.83 (+0%) | 2.45 (+0%) | 4.22 (+0%) | 3.82 (+0%) | 3.93 (+0%) | 3.57 (+0%) | 13.8 (+0%) | 13.57 (+0%) |
| | | | | | | | x | 2.91 (+0%) | 2.92 (+0%) | 4.14 (+0%) | 3.85 (+0%) | 10.81 (+0%) | 13.26 (+0%) | 27.84 (+0%) | 22.85 (+0%) |
| 2 | | | x | | | | x | **0.02** (+0%) | **0** (+0%) | 0.24 (-14%) | **0.17** (-11%) | **0.02** (+0%) | **0** (+0%) | 0.65 (-26%) | 0.37 (-23%) |
| | | | x | | | x | | **0.02** (+0%) | **0** (+0%) | 0.25 (-11%) | **0.17** (-11%) | **0.02** (+0%) | **0** (+0%) | 0.68 (-23%) | 0.4 (-17%) |
| | x | | x | | | | | **0.02** (+0%) | 0.01 (+Inf%) | 0.28 (+0%) | 0.18 (-5%) | 0.04 (+100%) | **0** (+0%) | 0.74 (-16%) | 0.42 (-13%) |
| 3 | | | x | | | x | x | **0.02** (+0%) | **0** (+0%) | **0.22** (-21%) | **0.17** (-11%) | 0.04 (+100%) | **0** (+0%) | **0.62** (-30%) | **0.36** (-25%) |
| | | | x | | x | | x | **0.02** (+0%) | **0** (+0%) | 0.23 (-18%) | 0.18 (-5%) | **0.02** (+0%) | **0** (+0%) | 0.64 (-27%) | 0.37 (-23%) |
| | | x | x | | | | x | **0.02** (+0%) | **0** (+0%) | 0.25 (-11%) | 0.19 (+0%) | **0.02** (+0%) | **0** (+0%) | 0.64 (-27%) | 0.44 (-8%) |
| 4 | x | | x | | | x | x | 0.03 (+50%) | **0** (+0%) | 0.23 (-18%) | **0.17** (-11%) | 0.04 (+100%) | **0** (+0%) | 0.64 (-27%) | 0.44 (-8%) |
| | | | x | x | | x | x | **0.02** (+0%) | **0** (+0%) | 0.25 (-11%) | 0.2 (+5%) | **0.02** (+0%) | **0** (+0%) | 0.65 (-26%) | 0.41 (-15%) |
| | | | x | | x | x | x | **0.02** (+0%) | **0** (+0%) | 0.25 (-11%) | 0.18 (-5%) | **0.02** (+0%) | **0** (+0%) | 0.65 (-26%) | 0.39 (-19%) |
| 5 | x | | x | | x | x | x | **0.02** (+0%) | **0** (+0%) | 0.26 (-7%) | **0.17** (-11%) | 0.04 (+100%) | **0** (+0%) | 0.69 (-21%) | 0.44 (-8%) |
| | x | | x | x | | x | x | **0.02** (+0%) | **0** (+0%) | 0.26 (-7%) | 0.19 (+0%) | 0.04 (+100%) | **0** (+0%) | 0.69 (-21%) | 0.47 (-2%) |
| | | | x | x | x | x | x | **0.02** (+0%) | **0** (+0%) | 0.27 (-4%) | 0.2 (+5%) | **0.02** (+0%) | **0** (+0%) | 0.7 (-21%) | 0.46 (-4%) |
| 6 | x | | x | x | x | x | x | **0.02** (+0%) | **0** (+0%) | 0.28 (+0%) | 0.19 (+0%) | 0.04 (+100%) | **0** (+0%) | 0.74 (-16%) | 0.51 (+6%) |
| | | x | x | x | x | x | x | 0.04 (+100%) | **0** (+0%) | 0.31 (+11%) | 0.23 (+21%) | 0.04 (+100%) | **0** (+0%) | 0.81 (-8%) | 0.54 (+13%) |
| | x | x | x | x | | x | x | **0.02** (+0%) | **0** (+0%) | 0.29 (+4%) | 0.2 (+5%) | 0.06 (+200%) | **0** (+0%) | 0.82 (-7%) | 0.56 (+17%) |
| 7 | x | x | x | x | x | x | x | 0.04 (+100%) | **0** (+0%) | 0.33 (+18%) | 0.22 (+16%) | 0.07 (+250%) | **0** (+0%) | 0.87 (-1%) | 0.63 (+31%) |

**USING LOCAL SIFT EXPERT RESTRICTED TO 200 KEYPOINTS PER IMAGE**

| # | systems: safe | gabor | sift | lbp | hog | ntnu | vgg | Equal Error Rate (EER): NIR | VW | cross-sensor | all | FRR @ FAR=0.01%: NIR | VW | cross-sensor | all |
|---|---|---|---|---|---|---|---|---|---|---|---|---|---|---|---|
| 1 | | | x | | | | | 0.15 (+0%) | 0.31 (+0%) | 1.07 (+0%) | 0.81 (+0%) | 0.44 (+0%) | 0.76 (+0%) | 4.02 (+0%) | 2.57 (+0%) |
| | | | | | | x | | 2.83 (+0%) | 2.45 (+0%) | 4.22 (+0%) | 3.82 (+0%) | 3.93 (+0%) | 3.57 (+0%) | 13.8 (+0%) | 13.57 (+0%) |
| | | | | | | | x | 2.91 (+0%) | 2.92 (+0%) | 4.14 (+0%) | 3.85 (+0%) | 10.81 (+0%) | 13.26 (+0%) | 27.84 (+0%) | 22.85 (+0%) |
| 2 | | | x | | | | x | 0.18 (+20%) | 0.32 (+3%) | 0.7 (-35%) | 0.61 (-25%) | 0.47 (+7%) | 0.75 (-1.3%) | 2.76 (-31%) | 2.23 (-13%) |
| | | | x | | | x | | **0.14** (-7%) | 0.28 (-10%) | 0.67 (-37%) | 0.58 (-28%) | 0.41 (-7%) | **0.62** (-18%) | 2.83 (-30%) | **2.17** (-16%) |
| | | | x | x | | | | 0.18 (+20%) | 0.36 (+16%) | 0.88 (-18%) | 0.82 (+1%) | 0.39 (-11%) | 0.86 (+13%) | 3.27 (-19%) | 2.58 (+0.4%) |
| 3 | | | x | | | x | x | 0.21 (+40%) | **0.24** (-23%) | **0.61** (-43%) | **0.6** (-26%) | 0.61 (+39%) | 0.8 (+5%) | **2** (-50%) | 2.25 (-13%) |
| | | | x | x | | x | | 0.17 (+13%) | 0.27 (-13%) | 0.68 (-36%) | 0.64 (-21%) | **0.38** (-14%) | 0.74 (-3%) | 2.46 (-39%) | 2.26 (-12%) |
| | | | x | | x | x | | 0.2 (+33%) | 0.27 (-13%) | 0.71 (-34%) | 0.62 (-24%) | 0.66 (+50%) | 0.78 (+3%) | 2.5 (-38%) | 2.27 (-12%) |
| 4 | | | x | x | | x | x | 0.26 (+73%) | 0.32 (+3%) | 0.73 (-32%) | 0.75 (-7%) | 0.64 (+46%) | 0.97 (+28%) | 2.19 (-46%) | 2.67 (+4%) |
| | | | x | | x | x | x | 0.3 (+100%) | 0.36 (+16%) | 0.77 (-28%) | 0.69 (-15%) | 0.8 (+82%) | 1.07 (+41%) | 2.46 (-39%) | 2.53 (-2%) |
| | | | x | x | x | x | | 0.3 (+100%) | 0.38 (+23%) | 0.84 (-22%) | 0.8 (-1%) | 0.72 (+64%) | 1 (+32%) | 2.51 (-38%) | 2.54 (-1%) |
| 5 | | | x | x | x | x | x | 0.39 (+160%) | 0.46 (+48%) | 0.9 (-16%) | 0.89 (+10%) | 0.8 (+82%) | 1.32 (+74%) | 2.82 (-30%) | 3.13 (+22%) |
| | | x | x | x | | x | x | 0.32 (+113%) | 0.46 (+48%) | 0.94 (-12%) | 0.93 (+15%) | 0.8 (+82%) | 1.24 (+63%) | 2.86 (-29%) | 3.15 (+23%) |
| | x | | x | | x | x | x | 0.46 (+207%) | 0.49 (+58%) | 1.1 (+3%) | 0.93 (+15%) | 1.06 (+141%) | 1.32 (+74%) | 2.87 (-29%) | 2.74 (+7%) |
| 6 | x | | x | x | x | x | x | 0.48 (+220%) | 0.64 (+107%) | 1.12 (+5%) | 1.06 (+31%) | 1.06 (+141%) | 1.45 (+91%) | 3.28 (-18%) | 3.31 (+29%) |
| | | x | x | x | x | x | x | 0.56 (+273%) | 0.56 (+81%) | 1.07 (+0%) | 1.06 (+31%) | 0.84 (+91%) | 1.36 (+79%) | 3.42 (-15%) | 3.17 (+23%) |
| | x | x | x | x | | x | x | 0.52 (+247%) | 0.52 (+68%) | 1.16 (+8%) | 1.07 (+32%) | 1.04 (+136%) | 1.4 (+84%) | 3.53 (-12%) | 3.44 (+34%) |
| 7 | x | x | x | x | x | x | x | 0.66 (+340%) | 0.74 (+139%) | 1.18 (+10%) | 1.13 (+40%) | 1.16 (+164%) | 1.5 (+97%) | 3.82 (-5%) | 3.5 (+36%) |

Table 5: Cross-Eyed database, test set (part 1): Verification results for an increasing number of fused systems. The best combinations are chosen based on the lowest FRR @ FAR=0.01% of cross-sensor experiments. The best result of each column is marked in bold. The relative variation with respect to the best individual system is also given in brackets.

**WITHOUT LOCAL SIFT EXPERT**

| # | systems | | | | | | | | Equal Error Rate (EER) | | | | FRR @ FAR=0.01% | | | |
|---|---|---|---|---|---|---|---|---|---|---|---|---|---|---|---|---|
| | **safe** | **gabor** | **sift** | **lbp** | **hog** | **ntnu** | **vgg** | | NIR | VW | cross-sensor | all | NIR | VW | cross-sensor | all |
| 1 | | | | | | x | | | 2.83 (+0%) | 2.45 (+0%) | 4.22 (+0%) | 3.82 (+0%) | **3.93** (+0%) | **3.57** (+0%) | 13.8 (+0%) | 13.57 (+0%) |
| | | | | | | | x | | 2.91 (+0%) | 2.92 (+0%) | 4.14 (+0%) | 3.85 (+0%) | 10.81 (+0%) | 13.26 (+0%) | 27.84 (+0%) | 22.85 (+0%) |
| | | | | | x | | | | 3.84 (+0%) | 4.19 (+0%) | 5.06 (+0%) | 4.84 (+0%) | 11.76 (+0%) | 14.93 (+0%) | 34.36 (+0%) | 30.05 (+0%) |
| 2 | | | | | x | x | | | 2.95 (+4%) | 2.6 (+6%) | 3.38 (-20%) | 3.33 (-13%) | 4.07 (+4%) | 4.33 (+21%) | 8.85 (-36%) | 9.71 (-28%) |
| | | | | | | x | x | | **2.01** (-29%) | **1.62** (-34%) | **2.58** (-38%) | **2.51** (-34%) | 4.44 (+13%) | 4.23 (+19%) | 9.38 (-32%) | 10.28 (-24%) |
| | | | | x | | x | | | 2.26 (-20%) | 2.13 (-13%) | 3.3 (-22%) | 3.31 (-13%) | 4.03 (+3%) | 3.89 (+9%) | 11.09 (-20%) | 15.65 (+15%) |
| 3 | | | | | x | x | x | | 2.35 (-17%) | 1.85 (-25%) | 2.83 (-32%) | 2.66 (-30%) | 4.33 (+10%) | 4.88 (+37%) | **8.8** (-36%) | 10.52 (-23%) |
| | | | | x | | x | x | | 2.05 (-28%) | 1.8 (-27%) | 2.86 (-31%) | 2.76 (-28%) | 4.35 (+11%) | 4.61 (+29%) | 9.88 (-28%) | 11.89 (-12%) |
| | | | | x | x | x | | | 2.69 (-5%) | 2.45 (+0%) | 3.34 (-21%) | 3.2 (-16%) | 4.27 (+9%) | 4.83 (+35%) | 9.99 (-28%) | 14.32 (+6%) |
| 4 | | | | x | x | x | x | | 2.27 (-20%) | 1.97 (-20%) | 2.89 (-30%) | 2.81 (-26%) | 4.17 (+6%) | 4.9 (+37%) | 9.52 (-31%) | 9.88 (-27%) |
| | | x | | x | x | x | | | 2.75 (-3%) | 2.41 (-2%) | 3.42 (-19%) | 3.32 (-13%) | 4.67 (+19%) | 5.26 (+47%) | 11.07 (-20%) | 14.71 (+8%) |
| | x | | | | x | x | x | | 2.01 (-29%) | 1.69 (-31%) | 3.02 (-27%) | 2.72 (-29%) | 4.82 (+23%) | 5.92 (+66%) | 11.15 (-19%) | 10.22 (-25%) |
| 5 | x | | | x | x | x | x | | 2.07 (-27%) | 1.74 (-29%) | 3.11 (-25%) | 2.85 (-25%) | 4.61 (+17%) | 5.12 (+43%) | 10.32 (-25%) | 9.36 (-31%) |
| | | x | | x | x | x | x | | 2.4 (-15%) | 2.13 (-13%) | 3.12 (-25%) | 3.1 (-19%) | 4.17 (+6%) | 4.96 (+39%) | 11.14 (-19%) | 9.33 (-31%) |
| | x | x | | x | x | x | | | 2.44 (-14%) | 2.03 (-17%) | 3.53 (-16%) | 3.23 (-15%) | 5.02 (+28%) | 6.2 (+74%) | 12.33 (-11%) | 12.78 (-6%) |
| 6 | x | x | | x | x | x | x | | 2.29 (-19%) | 1.91 (-22%) | 3.09 (-25%) | 2.96 (-23%) | 4.49 (+14%) | 5 (+40%) | 11.85 (-14%) | **8.83** (-35%) |

Table 6: Cross-Eyed database, test set (part 2): Verification results for an increasing number of fused systems. The best combinations are chosen based on the lowest FRR @ FAR=0.01% of cross-sensor experiments. The best result of each column is marked in bold. The relative variation with respect to the best individual system is also given in brackets.

| approach | safe | gabor | sift | lbp | hog | Training set EER | Training set GF2 | Test set EER | Test set GF2 | Competition [16] EER | Competition [16] GF2 |
|---|---|---|---|---|---|---|---|---|---|---|---|
| HH3 | | x | | x | x | 4.5 | 16.77 | 4.86 | 24.59 | 6.02 | 11.42 |
| HH2 | x | x | | x | x | 3.02 | 12.63 | 4.51 | 19.75 | 5.24 | 9.14 |
| HH1 | x | x | x | x | x | 0 | 0 | 0.28 | 0.83 | 0.29 | 0 |

Table 7: Comparison with results of the Cross-Eyed 2016 Competition. GF2 stands for FRR @ FAR=0.01%

**WITHOUT LOCAL SIFT EXPERT - BEST RESULT ACHIEVABLE BY ACCESS TYPE**

| **Equal Error Rate (EER)** | | | |
|---|---|---|---|
| NIR | VW | cross-sensor | all |
| 1.76 (-38%) | 1.62 (-34%) | 2.58 (-38%) | 2.51 (-34%) |

| **FRR @ FAR=0.01%** | | | |
|---|---|---|---|
| NIR | VW | cross-sensor | all |
| 3.93 (+0%) | 3.57 (+0%) | 8.8 (-36%) | 8.83 (-35%) |

Table 8: Cross-Eyed database, test set: best results achievable by access type. The relative variation with respect to the best individual system is also given in brackets.

| **VSSIRIS database** | | |
|---|---|---|
| **Comparison type** | | **Protocol** (28 subjects) |
| Same-sensor | Genuine | 56 $\times$ (4+3+2+1) = 560 |
| | Impostor | 56 $\times$ 55 = 3,080 |
| Cross-sensor | Genuine | 56 $\times$ 5 $\times$ 5 = 1,400 |
| | Impostor | 56$\times$ 55 = 3,080 |

Table 9: VSSIRIS database: Experimental protocol.

| | Equal Error Rate (EER) | | | | FRR @ FAR=0.01% | | | |
|---|---|---|---|---|---|---|---|---|
| | Same sensor | | | | Same sensor | | | |
| **system** | **iPhone** | **Nokia** | **cross-sensor** | **all** | **iPhone** | **Nokia** | **cross-sensor** | **all** |
| SAFE | 1.6% | 2.6% | 10.2% (+537.5%) | 7.5% | 4.6% | 11.1% | 50.9% (+1006.5%) | 36.3% |
| GABOR | 2.1% | 1.5% | 7.3% (+386.7%) | 5.8% | 4.3% | 8.9% | 39.1% (+809.3%) | 32.9% |
| SIFT | 0% | 0.1% | 1.6% (+Inf) | 0.8% | 0% | 0.7% | 12.7% (+Inf) | 7.2% |
| SIFT-200p | 0% | 0.8% | 6.6% (+Inf) | 5% | 0% | 2% | 41.9% (+Inf) | 23.7% |
| LBP | 4.8% | 4.9% | 14.1% (+193.8%) | 13.8% | 6.8% | 16.8% | 71.2% (+947.1%) | 61% |
| HOG | 3.9% | 4.5% | 11% (+182.1%) | 9.2% | 5.2% | 17.3% | 70.7% (+1259.6%) | 54.5% |
| NTNU | 0.7% | 0.7% | 4.1% (+480%) | 2.8% | 0.9% | 1.8% | 23.1% (+2500%) | 17.3% |
| VGG | 0.8% | 0.5% | 5.1% (+869.8%) | 3.8% | 2% | 1.8% | 24.4% (+1264.8%) | 16.2% |

Table 10: VSSIRIS database: Verification results of the individual systems. The relative variation of cross-sensor performance with respect to the best same-sensor performance is given in brackets.

**USING ALL THE SYSTEMS AVAILABLE**

| # | systems: safe | gabor | sift | lbp | hog | ntnu | vgg | Equal Error Rate (EER): iPhone | Nokia | cross-sensor | all | FRR @ FAR=0.01%: iPhone | Nokia | cross-sensor | all |
|---|---|---|---|---|---|---|---|---|---|---|---|---|---|---|---|
| 1 | | | x | | | | | **0** (0%) | 0.1 (0%) | 1.6 (0%) | 0.8 (0%) | **0** (0%) | 0.7 (0%) | 12.7 (0%) | 7.2 (0%) |
| | | | | | | x | | 0.7 (0%) | 0.7 (0%) | 4.1 (0%) | 2.8 (0%) | 0.9 (0%) | 1.8 (0%) | 23.1 (0%) | 17.3 (0%) |
| | | | | | | | x | 0.8 (0%) | 0.5 (0%) | 5.1 (0%) | 3.8 (0%) | 2 (0%) | 1.8 (0%) | 24.4 (0%) | 16.2 (0%) |
| 2 | | | x | | | | x | **0** (0%) | **0** (-100%) | **1** (-38%) | **0.5** (-38%) | **0** (0%) | **0** (-100%) | 4.2 (-67%) | 3.1 (-57%) |
| | | | x | | | x | | **0** (0%) | **0** (-100%) | **1** (-38%) | **0.5** (-38%) | **0** (0%) | **0** (-100%) | 5.1 (-60%) | 3.3 (-54%) |
| | | x | x | | | | | **0** (0%) | **0** (-100%) | 1.7 (+6%) | 0.8 (0%) | **0** (0%) | 0.2 (-71%) | 6 (-53%) | 3.4 (-53%) |
| 3 | | | x | | | x | x | **0** (0%) | **0** (-100%) | **1** (-38%) | **0.5** (-38%) | **0** (0%) | **0** (-100%) | 3.6 (-72%) | 2 (-72%) |
| | | x | x | | | x | | **0** (0%) | **0** (-100%) | 1.3 (-19%) | 0.7 (-13%) | **0** (0%) | **0** (-100%) | 4.1 (-68%) | 2.3 (-68%) |
| | | | x | | x | x | | **0** (0%) | **0** (-100%) | 1.3 (-19%) | 0.7 (-13%) | **0** (0%) | **0** (-100%) | 4.1 (-68%) | 3.6 (-50%) |
| 4 | x | | x | | | x | x | **0** (0%) | **0** (-100%) | **1** (-38%) | 0.6 (-25%) | **0** (0%) | **0** (-100%) | **3.4** (-73%) | **1.9** (-74%) |
| | | x | x | | | x | x | **0** (0%) | **0** (-100%) | 1.6 (0%) | 0.9 (+13%) | **0** (0%) | **0** (-100%) | 3.6 (-72%) | 2.1 (-71%) |
| | x | | x | | x | x | | **0** (0%) | **0** (-100%) | 1.2 (-25%) | 0.7 (-13%) | **0** (0%) | **0** (-100%) | 3.6 (-72%) | 2 (-72%) |
| 5 | | x | x | x | | x | x | **0** (0%) | **0** (-100%) | 2.1 (+31%) | 1.1 (+38%) | **0** (0%) | **0** (-100%) | 4.1 (-68%) | 2.5 (-65%) |
| | | x | x | | x | x | x | **0** (0%) | **0** (-100%) | 2 (+25%) | 1.3 (+63%) | **0** (0%) | **0** (-100%) | 4.2 (-67%) | 2.3 (-68%) |
| | x | x | x | | x | x | | **0** (0%) | **0** (-100%) | 1.8 (+13%) | 1.1 (+38%) | **0** (0%) | **0** (-100%) | 4.2 (-67%) | 2.5 (-65%) |
| 6 | | x | x | x | x | x | x | **0** (0%) | **0** (-100%) | 2.1 (+31%) | 1.3 (+63%) | **0** (0%) | **0** (-100%) | 4.6 (-64%) | 2.7 (-63%) |
| | x | x | x | x | | x | x | **0** (0%) | **0** (-100%) | 2 (+25%) | 1.2 (+50%) | **0** (0%) | **0** (-100%) | 4.6 (-64%) | 2.7 (-63%) |
| | x | x | x | | x | x | x | **0** (0%) | **0** (-100%) | 2 (+25%) | 1.2 (+50%) | **0** (0%) | **0** (-100%) | 4.7 (-63%) | 2.8 (-61%) |
| 7 | x | x | x | x | x | x | x | **0** (0%) | **0** (-100%) | 2.1 (+31%) | 1.4 (+75%) | **0** (0%) | **0** (-100%) | 5.2 (-59%) | 3.6 (-50%) |

**USING LOCAL SIFT EXPERT RESTRICTED TO 200 KEYPOINTS PER IMAGE**

| # | systems: safe | gabor | sift | lbp | hog | ntnu | vgg | Equal Error Rate (EER): iPhone | Nokia | cross-sensor | all | FRR @ FAR=0.01%: iPhone | Nokia | cross-sensor | all |
|---|---|---|---|---|---|---|---|---|---|---|---|---|---|---|---|
| 1 | | | | | | x | | 0.7 (0%) | 0.7 (0%) | 4.1 (0%) | 2.8 (0%) | 0.9 (0%) | 1.8 (0%) | 23.1 (0%) | 17.3 (0%) |
| | | | | | | | x | 0.8 (0%) | 0.5 (0%) | 5.1 (0%) | 3.8 (0%) | 2 (0%) | 1.8 (0%) | 24.4 (0%) | 16.2 (0%) |
| | | x | | | | | | 2.1 (0%) | 1.5 (0%) | 7.3 (0%) | 5.8 (0%) | 4.3 (0%) | 8.9 (0%) | 39.1 (0%) | 32.9 (0%) |
| 2 | | | x | | | x | | **0** (0%) | 0.2 (-71%) | **1.5** (-63%) | **1.3** (-54%) | **0** (0%) | 1.4 (-22%) | 9.6 (-58%) | 12.7 (-27%) |
| | | | | | | x | x | 0.7 (0%) | 0.3 (-40%) | 3.7 (-10%) | 2.6 (-7%) | 1.1 (+22%) | 0.9 (-50%) | 11.5 (-50%) | 15 (-7%) |
| | | | | | x | x | | 0.9 (+29%) | 0.6 (-14%) | 4.4 (+7%) | 3.1 (+11%) | 1.4 (+56%) | 1.4 (-22%) | 12.6 (-45%) | 14.2 (-18%) |
| 3 | | | x | | | x | x | **0** (0%) | **0.1** (-80%) | 1.6 (-61%) | **1.3** (-54%) | **0** (0%) | **0.5** (-72%) | **8** (-65%) | **10.9** (-33%) |
| | | | x | | x | x | | **0** (0%) | 0.3 (-57%) | 2 (-51%) | 1.6 (-43%) | **0** (0%) | 1.3 (-28%) | 9 (-61%) | 14.8 (-14%) |
| | | | x | x | | x | | **0** (0%) | 0.2 (-71%) | 2.1 (-49%) | 1.7 (-39%) | **0** (0%) | 1.4 (-22%) | 10.6 (-54%) | 16.2 (-6%) |
| 4 | | | x | | x | x | x | **0** (0%) | 0.2 (-60%) | 2.3 (-44%) | 1.7 (-39%) | 0.2 (+Inf) | **0.5** (-72%) | 8.4 (-64%) | 12.3 (-24%) |
| | | | x | x | | x | x | **0** (0%) | 0.2 (-60%) | 2.5 (-39%) | 1.8 (-36%) | 0.2 (+Inf) | **0.5** (-72%) | 9.1 (-61%) | 13.3 (-18%) |
| | | | x | x | x | x | | **0** (0%) | 0.4 (-43%) | 2.5 (-39%) | 2.3 (-18%) | **0** (0%) | 1.4 (-22%) | 9.4 (-59%) | 17.5 (+1%) |
| 5 | | | x | x | x | x | x | 0.2 (+Inf) | 0.2 (-60%) | 2.9 (-29%) | 2.1 (-25%) | 0.4 (+Inf) | **0.5** (-72%) | 9 (-61%) | 12.2 (-25%) |
| | | x | x | | x | x | x | 0.2 (+Inf) | 0.3 (-40%) | 2.8 (-32%) | 2 (-29%) | 0.2 (+Inf) | **0.5** (-72%) | 10.1 (-56%) | 9.8 (-40%) |
| | x | | x | | x | x | x | 0.2 (+Inf) | 0.2 (-60%) | 2.4 (-41%) | 1.8 (-36%) | 0.2 (+Inf) | **0.5** (-72%) | 10.6 (-54%) | 11 (-32%) |
| 6 | | x | x | x | x | x | x | 0.2 (+Inf) | 0.4 (-20%) | 3.3 (-20%) | 2.3 (-18%) | 0.5 (+Inf) | **0.5** (-72%) | 11.1 (-52%) | 10 (-38%) |
| | x | | x | x | x | x | x | 0.2 (+Inf) | 0.4 (-20%) | 3 (-27%) | 2.2 (-21%) | 0.2 (+Inf) | **0.5** (-72%) | 11.3 (-51%) | 10.9 (-33%) |
| | x | x | x | | x | x | x | 0.2 (+Inf) | 0.4 (-20%) | 2.9 (-29%) | 2 (-29%) | 0.2 (+Inf) | **0.5** (-72%) | 12.8 (-45%) | **9.1** (-44%) |
| 7 | x | x | x | x | x | x | x | 0.2 (+Inf) | 0.4 (-20%) | 3.1 (-24%) | 2.5 (-11%) | 0.8 (+Inf) | **0.5** (-72%) | 13.6 (-41%) | 9.3 (-43%) |

Table 11: VSSIRIS database (part 1): Verification results for an increasing number of fused systems. The best combinations are chosen based on the lowest FRR @ FAR=0.01% of cross-sensor experiments. The best result of each column is marked in bold. The relative variation with respect to the best individual system is also given in brackets.

**WITHOUT LOCAL SIFT EXPERT**

| # | systems | | | | | | | | Equal Error Rate (EER) | | | | FRR @ FAR=0.01% | | | |
|---|---|---|---|---|---|---|---|---|---|---|---|---|---|---|---|---|
| | **safe** | **gabor** | **sift** | **lbp** | **hog** | **ntnu** | **vgg** | | iPhone | Nokia | cross-sensor | all | iPhone | Nokia | cross-sensor | all |
| 1 | | | | | | x | | | **0.7** (0%) | 0.7 (0%) | 4.1 (0%) | 2.8 (0%) | **0.9** (0%) | 1.8 (0%) | 23.1 (0%) | 17.3 (0%) |
| | | | | | | | x | | 0.8 (0%) | 0.5 (0%) | 5.1 (0%) | 3.8 (0%) | 2 (0%) | 1.8 (0%) | 24.4 (0%) | 16.2 (0%) |
| | | x | | | | | | | 2.1 (0%) | 1.5 (0%) | 7.3 (0%) | 5.8 (0%) | 4.3 (0%) | 8.9 (0%) | 39.1 (0%) | 32.9 (0%) |
| 2 | | | | | | x | x | | **0.7** (0%) | **0.3** (-40%) | **3.7** (-10%) | **2.6** (-7%) | 1.1 (+22%) | **0.9** (-50%) | 11.5 (-50%) | 15 (-7%) |
| | | | | | x | x | | | 0.9 (+29%) | 0.6 (-14%) | 4.4 (+7%) | 3.1 (+11%) | 1.4 (+56%) | 1.4 (-22%) | 12.6 (-45%) | 14.2 (-18%) |
| | | | | x | | x | | | 1.4 (+100%) | 0.7 (0%) | 5.1 (+24%) | 3.7 (+32%) | 2.3 (+156%) | 1.6 (-11%) | 16.6 (-28%) | 18.1 (+5%) |
| 3 | | | | | x | x | x | | **0.7** (0%) | 0.4 (-20%) | 4.1 (0%) | 2.8 (0%) | 1.4 (+56%) | 1.1 (-39%) | **10.8** (-53%) | 12.2 (-25%) |
| | | | | x | | x | x | | 1.2 (+71%) | **0.3** (-40%) | 4.4 (+7%) | 3.1 (+11%) | 2.1 (+133%) | 1.1 (-39%) | 12.1 (-48%) | 15.9 (-2%) |
| | | x | | | | x | x | | **0.7** (0%) | 0.5 (0%) | 4.1 (0%) | 2.8 (0%) | 1.6 (+78%) | 1.1 (-39%) | 13.3 (-42%) | 14.8 (-9%) |
| 4 | | | | x | x | x | x | | 1.6 (+129%) | 0.5 (0%) | 4.9 (+20%) | 3.5 (+25%) | 2.1 (+133%) | 1.1 (-39%) | 14.1 (-39%) | 14.8 (-9%) |
| | | x | | | x | x | x | | 0.9 (+29%) | 0.6 (+20%) | 4.4 (+7%) | 3.1 (+11%) | 1.8 (+100%) | 1.1 (-39%) | 14.4 (-38%) | 13.2 (-19%) |
| | | x | | x | | x | x | | 1.4 (+100%) | 0.5 (0%) | 4.6 (+12%) | 3.3 (+18%) | 2.1 (+133%) | 1.1 (-39%) | 14.7 (-36%) | 15.2 (-6%) |
| 5 | | x | | x | x | x | x | | 1.6 (+129%) | 0.6 (+20%) | 4.9 (+20%) | 3.6 (+29%) | 2.1 (+133%) | 1.1 (-39%) | 17.6 (-24%) | 13.7 (-15%) |
| | x | x | | x | | x | x | | 1.1 (+57%) | 0.5 (0%) | 4.6 (+12%) | 3.3 (+18%) | 2.1 (+133%) | 1.3 (-28%) | 17.8 (-23%) | 13.1 (-19%) |
| | x | x | | | x | x | x | | **0.7** (0%) | 0.5 (0%) | 4.3 (+5%) | 3.2 (+14%) | 1.7 (+89%) | 1.1 (-39%) | 18.2 (-21%) | 12.6 (-22%) |
| 6 | x | x | | x | x | x | x | | 1.5 (+114%) | 0.5 (0%) | 4.9 (+20%) | 3.6 (+29%) | 2.1 (+133%) | 1.1 (-39%) | 20.3 (-12%) | **12** (-26%) |

Table 12: VSSIRIS database (part 2): Verification results for an increasing number of fused systems. The best combinations are chosen based on the lowest FRR @ FAR=0.01% of cross-sensor experiments. The best result of each column is marked in bold. The relative variation with respect to the best individual system is also given in brackets.

**WITHOUT LOCAL SIFT EXPERT - BEST RESULT ACHIEVABLE BY ACCESS TYPE**

| **Equal Error Rate (EER)** | | | |
|---|---|---|---|
| iPhone | Nokia | cross-sensor | all |
| 0.7 (+0%) | 0.2 (-71%) | 3.5 (-15%) | 2.6 (-7%) |

| **FRR @ FAR=0.01%** | | | |
|---|---|---|---|
| iPhone | Nokia | cross-sensor | all |
| 0.9 (+0%) | 0.9 (-50%) | 10.8 (-53%) | 12 (-26%) |

Table 13: VSSIRIS database: best results achievable by access type. The relative variation with respect to the best individual system is also given in brackets.